

**SCIENTIA EST  
POTENTIA**

KNOWLEDGE IS POWER



**ON  
THE  
COVER**

DESIGNED BY IRENE XIE

The front cover features a stylized cutout of the Earth, spanning from the core below to the cosmos above. It is incredible to think that all of science as we know it lies between these borders of Earth, sky, and stars, from the depth of the oceans to the darkness of deep space; to know that every cell ever studied only existed on one thin strip of green. From the troposphere to the final frontiers, this is our view of the known universe; and yet, there is always more to explore.



**THE  
2011-2012  
MSURJ  
COMMITTEE**

MCGILL SCIENCE UNDERGRADUATE RESEARCH JOURNAL 805 SHERBROOKE ST. WEST ROOM 1B21 MONTREAL, QUEBEC, H3A 2K6 CANADA

**EDITOR-IN-CHIEF**

ERIC ZHAO (PHYSICS & PHYSIOLOGY)

**MANAGING EDITOR**

YUHAO SHI (BIOLOGY)

**ASSOCIATE EDITORS**

NATALIE GOTTLIEB (PSYCHOLOGY)

DEBBIE WANG (NEUROSCIENCE)

**SENIOR EDITORS**

JANINE HSU (PHYSIOLOGY)

MIRANDA HUNTER (ANATOMY & CELL BIOLOGY)

LISA YANG (COGNITIVE SCIENCE)

**BOARD OF EDITORS**

BLAIR JIA (QUANTITATIVE BIOLOGY)

BRIAN KRUG (BIOLOGY)

SHANNON PALUS (PHYSICS)

JASSI PANNU (BIOLOGY)

KATHLEEN SHERIDAN (COGNITIVE SCIENCE)

ELAINE XIE (PHARMACOLOGY)

IRENE XIE (BIOCHEMISTRY & PHYSICS)

**ASSISTANT EDITOR**

AKSHAY RAJARAM (ANATOMY & CELL BIOLOGY)

**FACULTY OF SCIENCE ADVISOR**

VICTOR CHISHOLM (OFFICE FOR UNDERGRADUATE RESEARCH IN SCIENCE)

DR. SIMON YOUNG (PROFESSOR, DEPARTMENT OF PSYCHIATRY)

**LAYOUT DESIGNER**

ARLENE BAACO (ARLENE.BAACO@GMAIL.COM)

**GRAPHIC DESIGNER**

IRENE XIE

P. 514.398.6979  
F. 514.398.6766  
E. MCGILLSURJ@GMAIL.COM  
W. MSURJ.MCGILL.CA



<b>09</b>	FOREWORD
<b>11</b>	ACKNOWLEDGEMENTS
<b>13</b>	Anne Sophie Berg SCANNING THE COSMOS: THE SEARCH FOR LIFE IN THE UNIVERSE
<b>17</b>	Brian Chang RATTLING THE CORE OF A WELL-ESTABLISHED PARADIGM: IS RETINOIC ACID REALLY NECESSARY FOR MEIOSIS ENTRY?
<b>21</b>	Tiegan Hobbs, Fiona A. Darbyshire POINT ESTIMATES OF CRUSTAL THICKNESS USING RECEIVER FUNCTION STACKING
<b>28</b>	Clarence Leung BAYESIAN MODELS FOR PHYLOGENETIC TREES
<b>35</b>	Ningsi Mei AN ANALYTICAL METHOD DEVELOPMENT FOR THE STUDY OF CHEMICAL SPECIES OF MERCURY IN THE ATMOSPHERE
<b>42</b>	Tat Fong Ng, Mourad Matmati, Thomas M. Quinn PROTECTION OF THE DIFFERENTIATED CHONDROCYTE PHENOTYPE DURING MONOLAYER EXPANSION CULTURES USING HEAT INACTIVATED FETAL CALF SERUM
<b>49</b>	Akal Sethi GENOMICS OF REGULATORY ELEMENTS: A SPECIAL FOCUS ON THE HOXA GENE CLUSTER AND EXPERIMENTAL TECHNIQUES
<b>54</b>	Sophie Splawinski, John R. Gyakum, Dr. Eyad H. Atallah THE ROLE OF ANTICYLONES IN REPLENISHING SURFACE COLD AIR AND MODULATING FREEZING RAIN DURATION



## FOREWORD

DEAR READER,

As McGill University continues to polish its reputation as a world-class research institution, the McGill Science Undergraduate Research Journal (MSURJ) strives to nurture the seeds of research excellence by promoting research at the undergraduate level. With the publication of our seventh volume, we continue the proud tradition of encouraging students to communicate their contributions to science.

Since our inception in 2006, we have endeavoured to fulfill our mandate not just with our core publication, but also with community outreach events that expose the wondrous world of scientific research to CEGEP students in the Montreal area. This year marked the launch of The Abstract, an accessible science blog highlighting research by McGill professors. It is our goal to further scientific literacy and interest by coupling cutting-edge research with clear, engaging writing.

In this issue, we present to you the extraordinary works of students at McGill University. The subjects cover the full spectrum of scientific investigation, from bioinformatics to atmospheric science. The authors are undergraduate students who've demonstrated their investigatory prowess through summer research projects, thesis projects, and research coursework.

ERIC ZHAO

EDITOR-IN-CHIEF



## ACKNOWLEDGEMENTS

The publication of the seventh edition of the McGill Science Undergraduate Research Journal would not have been possible without the support of many individuals.

We thank Professor Martin Grant, Dean of the Faculty of Science, whose unwavering support throughout the past seven years has allowed this Journal to flourish.

We thank all of our donors in the McGill community for their generous support:

Science Undergraduate Student Society  
McGill Biology Student Union  
McGill School of Environment  
Faculty of Science

We also extend our gratitude to

Mr. Victor Chisholm for providing us with continued encouragement at every step of the way.

Dr. Simon Young of the Department of Psychiatry for offering valuable advice on the operations of the journal.

We wish to thank the professors and post-doctoral fellows who graciously offered their time to review students' article submissions.

We would like to acknowledge the tireless efforts of the MSURJ board of editors in assembling this edition of the journal. Lastly, we wish to recognize the student contributors whose commendable efforts have made this journal possible.



# Scanning the Cosmos: The Search for Life in the Universe

A.S. Berg\*<sup>1</sup>

<sup>1</sup>Department of Earth and Planetary Science, McGill University, 123 McGill College, Montreal, Quebec, Canada H3A1B1

## ABSTRACT

The utter vastness of the universe makes it seem possible, perhaps even very probable, that there is life thriving on other planets. The cosmos, governed everywhere by the same laws of nature, are teeming with the very material that composes the Sun, the Earth and human beings. Could there be other worlds like our own? Might life exist beyond this planet? To answer these questions, we must consider the specific environments and distinctive circumstances necessary for life to arise. With this information, the detection methods and tools able to scour the great expanse for signatures of life can be determined. They, in turn, can be utilized to gather further data, potentially leading to the discovery of new worlds and new beings.

---

## KEYWORDS

*Exoplanets, detection methods, extraterrestrial life*

\*Corresponding author:

anne-sophie.berg@mail.mcgill.ca

Received: 3 January, 2012

Revised: 2 March, 2012

## SCANNING THE COSMOS

### THE SEARCH FOR LIFE IN THE UNIVERSE

What is life? A seemingly simple question—yet a universally accepted, all-encompassing definition remains elusive. We must consider this fundamental question if we are to take on the challenge of searching for extraterrestrial life. Part of the challenge is that we have, for now, only one reference: Earth. Though terrestrial life seems impossibly diverse (consider the four biological families: archaea, bacteria, eukaryotes, viruses and all that they encompass), who is to say that life beyond our biosphere is not equally so, if not more? (1)

### LIFE AS WE KNOW IT

Life on Earth has been shown to be the result of matter organizing itself on various scales and under specific circumstances (2) over an extended period of time. Though the specific mechanisms from which life sprung remains a bone of contention, it is known that for life to develop, certain elements are needed: carbon, hydrogen, nitrogen, oxygen, phosphorus, and sulfur (3). These elements, created through the Big Bang and stellar evolution, form the backbone of life, and exist far and wide in our universe.

For life to prosper on a planet, a long-lasting energy source such as a star is required. Even if this requirement is met, life can only flourish in what is called the circumstellar habitable zone:

a range of distances within which the radiative output of the parent star allows for liquid water (4). The habitable zone of a star changes gradually with time—a consequence of stellar evolution. As the nuclear fusion processes that sustain stars begin to produce heavier elements, the central gas pressure changes. The star's output increases, which causes the star to become more luminous over time. This change in luminosity affects the habitable zone. The range of radial distances within which liquid water could be found throughout the entire lifetime of a star is called the continuously habitable zone (5). Life on Earth exists in the Sun's continuously habitable zone. Life on another planet would likely be found in a similar environment.

Additionally, the size of the star must be taken into consideration. More than ninety percent of stars are smaller than our Sun., These smaller stars are less luminous and thus the habitable zone lies closer to the star. Any planets orbiting within this region would become tidally locked to the star, plunging one half of the planet in perpetual frozen darkness and the other in constant scorching light. It is difficult to imagine life in what we would consider such an inhospitable setting. Yet let us not forget the extremophiles of our own planet, found in what are traditionally considered severely hostile environments to living beings. In the case of stars larger than our own, the problem that arises relates to time. The average lifetime of more massive stars is relatively short. Consequently, there may not be sufficient time for matter to organize and evolve into life. Overall, fewer than ten percent of stars in the universe are of a suitable mass to sustain life: between 0.7 and 1.7 solar masses (6).

## SHELTER FROM THE COSMOS

What of the planets themselves? Not all planets are created equal. Ergo not all planets provide safe havens for life. A typical star system contains rocky inner planets and gaseous outer planets. Rocky planets tend to be more favourable environments for life, as there exists the possibility of water on their surfaces (7). Many adhere to the theory that the first forms of life on Earth emerged from the primeval oceans. Therefore, importance has been placed upon finding water elsewhere in our solar system, our galaxy and the universe. Water, though necessary for life to arise, is not sufficient for life to thrive. A geologically active planet generates plate tectonics, which hold a crucial role in the carbon cycle. Moreover, geologic activity can provide protection for emerging life. The convective movement present within the molten outer core of such a planet produces a magnetic field that shields the planet and any emerging life forms from incoming solar and cosmic radiation (8).

Other factors important to the habitability of a planet are its orbit's eccentricity and obliquity (9). The amount of thermal energy a planet receives from a star on an annual basis is greatly influenced by the eccentricity of its orbit (a measure of the perihelion and aph-

elion distances). The more eccentric an orbit, the less hospitable the planet, and vice-versa. Obliquity, the angle between a planet's spin axes and its orbit, influences planetary climate. Depending on the degree of the angle, a planet could experience a multitude of different temperature conditions, some tailor-made to harbour life and others thoroughly unsuitable. An ideal obliquity is one that guarantees a climate befitting the survival of living organisms: not too hot, nor too cold. The obliquity of Earth is 23.5 degrees. Such an incline gives rise to the seasons, ensuring the habitability of all regions year-round. Hypothetically, if Earth's obliquity was more extreme, say near 90 degrees, a large area would become a barren wasteland. Still yet, there is the added influence of the obliquity's stability. Earth's obliquity has remained constant due to its steady relationship with the Moon, allowing life to flourish. Alternatively, the teetering obliquity of Mars (fluctuating between 0 and 60 degrees, currently 25 degrees) has produced a barren landscape, seemingly devoid of life.

Though life might seem to prefer rocky planets (like ours), do not discount the gas giants, for they have their use. In a planetary system, the gravitational influence of larger gaseous planets can reduce the incidence of comet and asteroid impacts (10) on the smaller inner planets. This is of significance, considering the frequency of such impacts in space (as evidenced by the multitude of craters on the surface of the moon) and the devastating destruction they can cause.

The development of life boils down to three key points: a stable source of energy such as stars, an Earth-like planet within the habitable zone and the presence of the elemental building blocks of life (C,H,N,O,P,S). One could consider these the framework of the practical search for life in the universe.

## LOOKING AND LISTENING

Despite our best efforts (direct imaging, rovers, in situ experiments of the Viking Mars Landers, etc.) even the most promising candidates for life in our solar system have yet to provide proof. Luckily, beyond our own planetary system lies a great deal more to be discovered. According to the online Interactive Extra-solar Planet Catalogue, as of January 2012, a little over 700 extra-solar planets have been detected. This is no easy feat considering planets are much smaller and dimmer than stars, and therefore practically impossible to detect directly. Ingeniously, astronomers have devised a series of indirect approaches by utilizing the effects that planetary bodies exert on the stars they orbit.

The most effective methods are radial velocity and transit photometry. Radial velocity exploits the concept of the Doppler effect. A star orbited by a body experiences a gravitational tug that causes the star to wobble in a small circle or ellipse. Using very sensitive spectrographs, a periodic shift in the star's spec-

trum can be observed: a blue-shift as the star wobbles toward the observer and a red-shift as it wobbles away. If these shifts are observed regularly, then this is evidence of an orbiting body, perhaps even a planet. This method provides an estimate of an orbiting body's minimum mass, which can determine the nature of the body, planet or otherwise. Unfortunately, this method tends to detect types of planets least likely to have conditions suitable for life since small earth-like planets cause a relatively smaller and less easily detected wobble than their giant gaseous counterparts (11).

Transit photometry measures the tiny dip in brightness of a star as a body passes in front of it. This body is most likely a planet if the diminished brightness moment occurs at regular intervals. The magnitude of the dip is proportional to the size of the transiting body. Combining mass and size data from both the radial velocity and transit methods provides information on the planet's density, which thus sheds light on its composition. Furthermore, the observed absorption spectrum of a transit infers the planet's atmospheric makeup (12). All this information provides key insights into the habitability of a planet.

A third method, microlensing, can be used at much greater distances than radial velocity and transit photometry – thousands of light years away. The immense range of this technique becomes apparent when you consider that Pluto is mere light *hours* from us, whereas the diameter of the Milky Way galaxy is *hundreds* of thousands of light years across. Microlensing is the practical application of Einstein's General Theory of Relativity, which predicts the distortion of light waves due to gravity. When a star passes in front of a more distant star, it will act as a lens, distorting the light waves and amplifying the brightness of the distant star (13). This amplification can last up to about a month, sometimes giving an orbiting planet enough time to reveal itself. In such cases, the telltale result is a momentary spike in brightness.

Astrometry is yet another indirect detection method. Similar to radial velocity, it infers the existence of an orbiting planet through the detection of a wobble. The distinction between the two techniques is that astrometry uses a star's wobble relative to its surrounding stars in the sky instead of to its orbiting bodies.

The detection methods described above demonstrate the creativity and enterprise present within the field of astronomy. However, they do not take into account the possibility of extraterrestrial intelligence equally imaginative and resourceful. We can painstakingly search the skies for planets like ours to get a better understanding of how hospitable our universe is, however, there may be a shortcut: If indeed there exist such beings elsewhere in the universe with similar cosmic agendas, then surely they would have, like us, harnessed the power of science and technology. Radio

astronomy, the study of radio waves emitted by distant objects (14), is an exciting tool in the search for extraterrestrial civilizations. Radio waves are not absorbed or scattered by interstellar gas, and thus can travel very large distances unimpeded (15). Listening for radio signals from space garners a significant amount of noise from all regions of the electromagnetic spectrum. Fortunately, within this spectrum lies a comparatively quiet zone: the 21 cm line. Hypothetical advanced civilizations could most certainly use this range for communication. Radiotelescopes calibrated to the 21 cm line and pointed toward extrasolar planets would certainly pick up any extraterrestrial chatter, though this has yet to prove fruitful. Radio astronomy is one of our greatest resources in the search for intelligent life forms in the universe.

The beauty of the pursuit for life in the cosmos lies within the process. The scanning of the skies breeds a plethora of new discoveries and achievements. These in turn give rise to further innovation. Though we may never discover extraterrestrial life forms or achieve contact with intelligent alien civilizations, the knowledge amassed on this cosmic journey is never squandered. We must persevere. Carl Sagan said it best: "Imagination will often carry us to worlds that never were. But without it we go nowhere."

## REFERENCES

1. C.E. Cleland, C.F. Chybna, *Origins Life Evol. Biosphere* **32**, 387 (2002).
2. C.E. Scharf, *Extrasolar Planets and Astrobiology* (Univ. Science Books, California, 2009), p.2.
3. M.L. Kutner, *Astronomy: A Physical Perspective* (Cambridge Univ. Press, New York, 2003), p. 540-541.
4. H.A. Smith, *American Scientist* **99**, 320 (2011).
5. C.E. Scharf, *Extrasolar Planets and Astrobiology* (Univ. Science Books, California, 2009), p.381-382.
6. H.A. Smith, *American Scientist* **99**, 320 (2011).
7. C. Brusso, *Ad Astra* **22**, 48 (2010).
8. H.A. Smith, *American Scientist* **99**, 320 (2011).
9. H.A. Smith, *American Scientist* **99**, 320 (2011).
10. C. Brusso, *Ad Astra* **22**, 48 (2010).
11. M.L. Kutner, *Astronomy: A Physical Perspective* (Cambridge Univ. Press, New York, 2003), p. 85-87.
12. C.E. Scharf, *Extrasolar Planets and Astrobiology* (Univ. Science Books, California, 2009), p.150.
13. M.L. Kutner, *Astronomy: A Physical Perspective* (Cambridge Univ. Press, New York, 2003), p. 144-145..
14. M.L. Kutner, *Astronomy: A Physical Perspective* (Cambridge Univ. Press, New York, 2003), p. 68.
15. C. Sagan, *Cosmos* (Wings Books, New York, 1995), p.297.



# Rattling the core of a well-established paradigm: is retinoic acid really necessary for meiosis entry?

Brian (Po-yen) Chang\*<sup>1</sup>

<sup>1</sup>Department of Anatomy and Cell Biology, McGill University, Montreal, Quebec, Canada

## ABSTRACT

Independent studies from recent years have yielded a wealth of evidence supporting the model that retinoic acid (RA) triggers the expression of Stimulated by retinoic acid 8 (Stra8) gene in germ cells thereby inducing their entry into meiosis (1, 2). Kumar et al.'s recent work published in 2011, however, boldly challenges this model, proposing that entry into meiosis, in fact, takes place independently of endogenous RA (3). This controversial claim has attracted intense interest in the field of developmental biology and has prompted several follow-up studies. One of these studies has proposed two homeobox genes, Msx1 and Msx2, to also be necessary for female meiosis initiation, and that their actions are likely mediated by the expression of Stra8 (4).

## KEYWORDS

*Retinoic acid- the proposed extrinsic inducer of Stra8 in the current model for meiosis entry*

*Meiosis entry- a critical, sex-specific process in spermatogenesis and oogenesis*

*Stra8- the unequivocal regulating factor of meiosis entry in male and female germ cells*

*Cyp26b1- a male-specific, RA-degrading enzyme that inhibits meiosis entry in the testis*

*Msx1, Msx2- two homeobox genes that have been recently proposed to regulate meiosis entry*

\*Corresponding author:

ccbrian@gmail.com

Received: 16 January, 2012

Revised: 2 March, 2012

## THE BIG QUESTION

Germ cells enter meiosis at dramatically different times between the sexes: female germ cells enter at around 13 days post-coitum (dpc), but male germ cells do not enter until postnatally, at around 7-10 days post-partum (dpp) (5). This observation frames the central question that many researchers are trying to answer: what determines the sex-specific difference in the timing of meiosis entry?

## THE CURRENT PARADIGM

Previous gene knockout studies have firmly established Stra8 as the unequivocal regulator of meiotic program initiation in both spermatogenesis and oogenesis. Indeed, male germ cells from pure C57BL/6 mice depleted of Stra8 gene function did not progress beyond the preleptotene stage (6). Additionally, while germ cells from mice of mixed genetic background were able to complete meiotic replication and enter meiosis, they failed to proceed past the prophase stage (6). Other studies that followed shortly after have confirmed this finding (7-10). In particular, the work of Menke et al. has determined a strong correlation between the wave of anterior-posterior expression of Stra8 and the wave of anterior-posterior expression of bona fide meiotic mark-

ers, such as synaptonemal complex protein 3 (Scp3) and Dmc1 [DMC1 dosage suppressor of mck1 homolog, meiosis-specific homologous recombination (yeast)] (10).

Previous studies have suggested that retinoic acid (RA), a vitamin A derivative, is the extrinsic inducer of Stra8 and is thus necessary for regulating the induction of meiosis (11). The very gene designation Stra8 is, in fact, an acronym for “stimulated by retinoic acid.” Thus far, RA and its underlying mechanisms of function have been well studied and documented. During embryonic development, RA commonly functions in a paracrine manner. Its local level is finely tuned by the balance between its tissue-specific synthesis by the retinaldehyde dehydrogenases (Raldh1, Raldh2, Raldh3) and its oxidative degradation by the cytochrome P450 enzymes (Cyp26a1, Cyp26b1, Cyp26c1) (12). Once generated, RAs then travel to RA-target cells where they directly regulate genes by binding to two families of nuclear receptors—RA receptors (RARs) and retinoid X receptors (RXRs)—bound to the RA response elements (RAREs) in the regulatory regions of their targeted genes (12). This general model applies differently to different organisms. In mice, evidence suggests that the expression of Raldh2 in the mesonephros serves as the main paracrine source of RA for the adjacent gonad, which does not express Raldh2 (13).

Several areas of study lend support to the necessity of RA in meiosis entry. Two in particular are relevant to this discussion. First, the exogenous treatment of RA is sufficient to stimulate Stra8 expression in embryonal carcinoma cells and embryonic stem cells in culture (14). Second, which was demonstrated more recently, exogenous RA can also stimulate germ cells in the embryonic testes to begin expressing Scp3, Dmc1, and member X ( $\gamma$ H2afx) of the H2A histone family, and undertake meiosis-specific morphology (11, 13, 15, 16).

Besides Stra8 and RA, the P450 enzyme Cyp26b1, normally expressed in Sertoli cells of fetal testis, is the third ingredient in the cocktail of factors essential for regulating entry into meiosis. Importantly, Cyp26b1 has been shown to act as a crucial masculinizing factor that delays meiosis entry in male mice (10, 13, 17, 18). When resident germ cells in male testis were treated with ketoconazole, a potent but non-specific cytochrome p450 inhibitor, expressions of Stra8, Scp3, and Dmc1 were upregulated and these cells proceeded to develop meiosis-specific morphology (11, 13). When these cells were treated simultaneously with ketoconazole and RAR panantagonist BMS-204493, however, meiotic induction ceased to take place. This suggests that ketoconazole, although a non-specific inhibitor of P450 enzymes, acts specifically through the RARs to induce meiosis. This finding lends support to previous studies, which postulated that Cyp26b1 acts to degrade RA. Other tests, including those involving a more specific inhibitor of Cyp26 enzymatic activity, R115866, as well as

its treatment in combination with the RAR panantagonist, produced parallel results (11).

Together, this large body of studies generated the most recent and widely-accepted model to explain the sex-specific timing of meiosis entry: RA synthesized in the mesonephros serves as an extrinsic inducer of Stra8 and hence meiosis entry in the adjacent gonad, unless degraded by Cyp26b1, as in the case of fetal testis.

## THE PERCEIVED KNOWLEDGE GAPS

Despite the wealth of evidence in support of the current model, Kumar et al. remained skeptical (3). In their discussion, they identify several weak links common to the recent studies. They point out that in the studies involving exogenous RA treatment, including that which led to the first identification of Stra8 as an RA-responsive gene, ‘supra-physiological’ concentrations were used, which clearly could not be reflective of the endogenous reality. They also raise concerns over findings from studies using the RAR antagonists, stating that they are known to exert non-specific effects on receptors other than the RARs (19). Additionally, they suggest that commonly used RALDH inhibitors for studying meiosis entry, including the disulfiram compounds Win18,446 and citral, are known to also inhibit other aldehyde dehydrogenases that have no relevance to retinoid metabolism (20). This means that such RALDH inhibitors are likely to produce artifacts and misinterpretations. Kumar et al., doubtful of the validity of the current model, set out to investigate further (3).

## THE RATTLING DISCOVERY

Kumar et al. (3) set out to determine whether endogenous RA is indeed, as proposed by the current model, necessary for the induction of meiosis entry. To investigate this link, they looked at meiosis in fetal ovary null for either Raldh2 alone or in combination with Raldh3. Surprisingly, despite the absence of these two major RA synthesizing enzymes, Stra8 was still expressed and bona fide meiosis markers Scp3 and  $\gamma$ H2AX protein were still detectable. This finding implies that meiosis had occurred normally. But was RA really absent in the fetal ovaries of these mutant mice? To test this, they used a transgenic RARE-LacZ mouse line to report the RA activity, and assuredly, they did not detect its level in the mesonephros or the developing ovary of the mutant mouse background. Further tests also confirmed that the RARE used in the RARE-LacZ reporter construct was indeed sensitive enough, at least more sensitive than the putative Stra RARE found in the endogenous system, to detect the endogenous level of RA.

Inhibition of Cyp26b1 in fetal mutant testes, which lack a source of putative Stra8-inducing RA from the adjacent mesonephros, still led to the induction of Stra8 expression. However, when the mesonephros was removed from the testes, Stra8 expression was not induced.

All these findings led Kumar et al. to two main conclusions: 1) Stra8 expression remains unaffected in the absence of RA in the fetal ovary and is therefore not required for the induction of meiosis during ovary development; 2) some extrinsic signal, other than RA, is required from the mesonephros to induce meiosis, and the role of Cyp26b1 is not to degrade endogenous RA, as proposed by the current model, but rather to block that non-retinoic, meiosis-inducing signal (3).

Kumar et al.'s findings have flared up a whirlwind of contention in the field of developmental biology. While some groups hail the new possibilities, other groups vehemently protect the integrity of the current model.

## THE PROTECTORS (21)

Griswold et al., for one, rest in favour of the current model and have offered alternative interpretations to Kumar et al.'s observations. First, in regards to the observation that meiosis could be induced in the absence of RA, they argued that there remains the possibility that RA persisted in Kumar et al.'s experimental system. Even though the mutant mice were null for the major RA producing enzymes, Raldh2 and Raldh3, Raldh1 was unaccounted for. Raldh1 is also capable of synthesizing RA and it could have been feeding out low amounts of RA, which in turn drove the meiosis in Kumar et al.'s system.

But if RA was present in the system, why was its activity undetected by the RARE-LacZ reporter construct? Kumar et al. clearly demonstrated that the technique is sensitive enough to detect the levels of RA required to induce Stra8 activity. To address this, Griswold et al. pointed to a recent study investigating the reliability of RARE-LacZ construct. This paper concluded that, although a powerful technique, RARE-LacZ remains prone to losing responder activity, which could lead to a failure in detecting RA (22).

Griswold et al. also questioned the reliability of Kumar's experimental system setup itself. To overcome the embryonic lethality associated with RA deficiency of the mutant mice null for the retinaldehyde dehydrogenases, Kumar et al. administered to these mice exogenous RA up to 9dpc before clearing it away. Griswold et al. argue that adding exogenous RA necessarily

complicated their experimental system and gave rise to unwanted possibilities that were unaccounted for in Kumar et al.'s study, such as delayed effects of early RA exposure that later trigger meiosis. Given that no quantitative evidence had been presented to prove that RA was indeed completely cleared from the gonads post-administration, the possibility that residual amounts of RA persisted at low levels in these systems cannot be discounted. Griswold et al. further contend that given the lack of evidence that Cyp26b1 can degrade non-retinoid compounds, the simplest explanation for Kumar et al.'s findings is that their observations are attributed to RA.

## THE HAILERS (4)

On the other end of the spectrum, other researchers are pushing to elucidate the implications of Kumar et al.'s findings. In particular, Livera et al.'s most recent publication proposed two new essential factors that regulate meiosis initiation: homeobox proteins Msx1 and Msx2. Until now, homeobox proteins have not been implicated in meiosis entry control. Msx homeobox proteins are important for the correct development of many organs, including the limbs, teeth, and neural crest (23).

Using the Msx1ERT2cre mice with a ROSAmT/mG reporter system, Livera et al. confirmed that Msx1 protein is expressed in germ cells in the fetal ovary at 13 dpc, suggesting a correlation between Msx gene expressions and female fetal meiosis initiation. Furthermore, the double knockout (dKO) of Msx1 and Msx2 prevented most germ cells in the female ovary from initiating meiosis. Msx genes appear to function specifically in female meiosis, having no detectable level of activity in males when meiosis begins in the post-natal testis. Other studies involving morphological observations of female germ cells that did not undergo meiosis demonstrated that Msx is likely required solely for the initiation step of meiosis, but not for its progression through prophase I. This was demonstrated by a subset of cells which had successfully initiated meiosis at 14.5 dpc in the dKO ovaries, and have progressed normally through meiosis to the diplotene stage.

More relevant to this discussion is Livera et al.'s observation that Stra8 could be a target of Msx proteins, as overexpression of Msx1 increased Stra8 expression and Msx1 was found to bind the Stra8 promoter. The time period during which Msx proteins are needed to act on Stra8 and the fact that other co-factors may be involved in the process, however, are questions that still need to be answered.

## WRAPPING UP

Evidently, studies into the role of homeobox genes in regulating meiosis initiation is at a premature stage, to say the least, and more questions were posed than were answered by Livera et al.'s work. Nevertheless, this report work presents a promising outlook on a new field of study waiting to emerge.

Furthermore, on the question of whether RA is indeed required for meiosis, the two pivotal works by Kumar et al. and Livera et al., along with other recent studies, certainly demonstrate that thus far, we have but an incomplete picture. Beyond the relationship between RA, Stra8 and meiosis initiation, many other factors and modulators are also involved, including DAZL, FGF9, and DMRT1, which have been recently identified. In the end, this is perhaps entirely expected of a critical developmental process that would ultimately result in the formation of the complex organisms that mammals are. Whatever the case may be, one thing is for certain: the study of regulation of meiosis entry has just begun, and these recent breakthroughs will pave the way for many more exciting discoveries to come.

## ACKNOWLEDGEMENTS

I wish to thank Dr. Hugh Clarke and Dr. David Dankort for guiding me in writing this paper.

## REFERENCES

1. C. A. Smith, K. N. Roeszler, J. Bowles, P. Koopman, A. H. Sinclair, *BMC Dev Biol* **8**, 85 (2008).
2. A. Wallacides, A. Chesnel, D. Chardard, S. Flament, H. Dumond, *Dev Dyn* **238**, 1389 (Jun, 2009).
3. S. Kumar et al., *Nat Commun* **2**, 151 (Jan 11, 2011).
4. G. Livera et al., *Development* **138**, 5393 (Dec, 2011).
5. A. McLaren, *Dev Biol* **262**, 1 (Oct 1, 2003).
6. E. L. Anderson et al., *Proc Natl Acad Sci U S A* **105**, 14976 (Sep 30, 2008).
7. Q. Zhou et al., *Biol Reprod* **78**, 537 (Mar, 2008).
8. Q. Zhou et al., *Biol Reprod* **79**, 35 (Jul, 2008).
9. M. Mark, N. B. Ghyselinck, P. Chambon, *Curr Opin Genet Dev* **14**, 591 (Oct, 2004).
10. D. B. Menke, J. Koubova, D. C. Page, *Dev Biol* **262**, 303 (Oct 15, 2003).
11. J. Koubova et al., *Proc Natl Acad Sci U S A* **103**, 2474 (Feb 21, 2006).
12. G. Duyster, *Cell* **134**, 921 (Sep 19, 2008).
13. J. Bowles et al., *Science* **312**, 596 (Apr 28, 2006).
14. M. Oulad-Abdelghani et al., *J Cell Biol* **135**, 469 (Oct, 1996).
15. G. MacLean, H. Li, D. Metzger, P. Chambon, M. Petkovich, *Endocrinology* **148**, 4560 (Oct, 2007).
16. E. Trautmann et al., *Cell Cycle* **7**, 656 (Mar 1, 2008).
17. H. Li, G. MacLean, D. Cameron, M. Clagett-Dame, M. Petkovich, *Plos One* **4**, (Oct 19, 2009).
18. A. E. Baltus et al., *Nat Genet* **38**, 1430 (Dec, 2006).
19. M. Schupp, J. C. Curtin, R. J. Kim, A. N. Billin, M. A. Lazar, *Mol Pharmacol* **71**, 1251 (May, 2007).
20. N. A. Sophos, V. Vasiliou, *Chem Biol Interact* **143-144**, 5 (Feb 1, 2003).
21. M. D. Griswold, C. A. Hogarth, J. Bowles, P. Koopman, *Biol Reprod*, (Nov 9, 2011).
22. Y. Sakai, U. C. Drager, *Methods Mol Biol* **652**, 277 (2010).
23. Y. Lallemand et al., *Development* **132**, 3003 (Jul, 2005).

# Point Estimates of Crustal Thickness Using Receiver Function Stacking

Tiegan Hobbs\*<sup>1</sup>, Fiona A. Darbyshire<sup>2</sup>

<sup>1</sup>Department of Earth and Planetary Sciences, McGill University, Montréal, Quebec

<sup>2</sup>Centre de Recherche GEOTOP, Université du Québec à Montréal, Montréal, Quebec

## ABSTRACT

**Introduction:** Through receiver function analysis, this study inquires into some of the most basic properties of the crust below Southern and Central Quebec. **Methods:** This is accomplished, using receiver function technique, by stacking waveforms from 277 teleseismic events magnitude 6.0 and larger to find the delay in arrival time for several phases of the P-wave coda, relative to the initial P-wave arrival. This information is used to establish a linear relationship between thickness and P- to S-wave velocity ratio, each of which is stacked for a given station to identify a best-fit estimate for depth to the Moho and Vp/Vs ratio. To determine their accuracy these results are compared with previous seismic studies, as well as synthetically generated receiver function P-wave arrivals based on simple 1D crustal models. Thickness calculations for the crust varied from 28 to 48 km; variation which was most likely the result of either complicated 3D structures or a shortage of available high-magnitude events for some stations. Most of the results fell within appropriate windows outlined by studies like LITHOPROBE. **Discussion:** Given that the 9 broadband stations used in this study compose an area from the Superior Province, Grenville Province and a selection of their subprovinces and intrusions, reliable evaluations of the crustal thicknesses below these seismic stations have broad relevance in understanding the crustal structure below Quebec.

## KEYWORDS

*Seismology: Study of waves of energy released by an earthquake (seismic event).*

*Receiver Function: Deconvolution of a three-component seismogram into one single file.*

*LITHOPROBE: Series of reflection seismology transects performed to characterize structure of crust in targeted areas across Canada.*

*Abitibi: Neoarchaean greenstone belt on Canadian Shield.*

\*Corresponding author:

tiegan.hobbs@gmail.com

Received: 2 January, 2012

Revised: 2 March, 2012

## INTRODUCTION

This project used seismograms recorded at a number of Quebec seismic stations, all of which are part of the Canadian National Seismic Network. These stations were set up in Belletierre (BELQ), Chibougamau (CHGQ), Dolbeau (DMCQ), La Tuque (LATQ), Lebel-sur-Quévillon (LSQQ), Matagami (MATQ), Nemaska/Némiscau (NEMQ/NMSQ), and Rénard Mine (YOSQ) as shown in Fig. 1. They overlie several interesting geological provinces in the region, covering orogenic and accretionary events dating as far back as the Neo- or Mesoproterozoic (approximately 2.7Ga). Estimates of crustal thickness below these stations are useful in characterizing the ‘topography’ of the crust-mantle interface, enhancing our understanding of how ancient tectonic events continue to shape and define the structure of our continent.

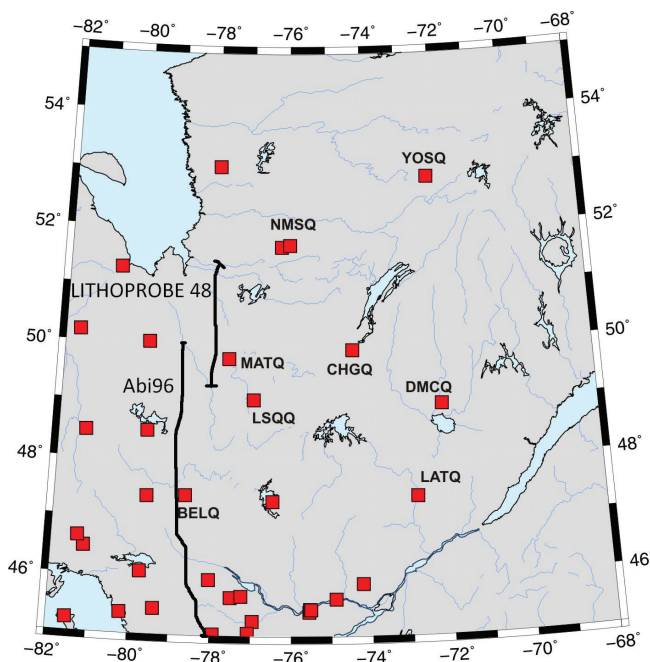


**Fig 1.** Map of study area with seismic stations indicated by red squares. Stations used in study are labelled. Approximate locations are shown for LITHOPROBE transect 48 and Abi96 line.

The Abitibi Greenstone belt, where MATQ, LSQQ, CHGQ, and BELQ stations are located, is in the Superior Province. It is a supracrustal Archaean belt composed of low-grade, regionally metamorphosed igneous and sedimentary rocks, which are mostly of mafic origin (as supported by the high  $V_p/V_s$  ratios for this region (1)). The term “greenstone” reflects the presence of the green minerals chlorite and actinolite. In 2007 it was determined that portions of the Abitibi are highly anisotropic: the minerals therein favour certain directions of wave propagation over others, resulting in differing wave travel times depending upon the incoming angle of the ray and the orientation of the station (1). Crustal thickness estimations in past studies conducted in the Abitibi, along LITHOPROBE transect 48 using seismic reflection profiles (2), did not exceed 40 km. The depth below the other seismic reflection line, Abi96 above 46.6°N, varied between 35 and 40 km according to a study conducted by Rondenay et al (3). Both of these works involved interpreting reflected seismic profiles by picking out key reflectors in the earth’s crust and connecting them into coherent layers. The current work, however, assumes a homogeneous single layer crust where the only seismic reflector to alter wave speed will be the Moho. Therefore the amount of complexity that can be perceived by reflection seismology depends on the interpreter, whereas in this refraction study there is little to no complexity assumed.

The YOSQ Station is contained in the Opinaca gneissic belt of the Superior Province, while NMSQ and NEMQ are in the 2850 Ma plutonic Opatica belt. The Superior is the world’s largest Archaean craton. Due to lack of seismic station coverage it has not previously been given a crustal thickness estimate.

Both LATQ and DMCQ are in the Grenville Province, part of the Grenville Orogeny that continues from eastern Canada into the central United States. It is a relic of a Himalayan-type continent-continent collision that occurred around 1 billion years ago following 800 million years of convergence at the southeast corner of the proto-continent Laurentia (2). Despite a lack of remaining mountainous terrain, there is a great deal of relic relief at the crust-mantle interface. Eaton et al. (4) published an estimate of crustal thickness in a further western part of the Grenville Province of between 34–52.4 km, while in 2000 Ludden and Hynes (2) published a narrower range of between 40 km in the north and 45 km in the south, on a line about 100 km southwest of LATQ.

## METHODS

This study uses the method of Zhu and Kanamori (5), stacking receiver functions (RFs) and comparing arrival times of P-wave transformations with the arrival of the initial P-wave. Receiver functions are created by deconvolving the vertical component from the radial (along path) and tangential components (at 90° to the direction of propagation) of a seismogram for a particular earthquake. Effectively, it turns three different axes of motion from each event into just one seismogram so one can more easily investigate several earthquakes at once. In particular, using RFs makes it easier to identify the incoming P-wave to S-wave conversions like Ps, PpPs, and the combined PpPs+PsPs, all of which involve conversions of seismic P- and S- waves as they interact with the crust-mantle boundary.

By comparing the difference in arrival times between any of these converted phases and the initial P-wave, we can determine the amount of time it takes a certain type of wave to traverse the thickness of the crust. With this information, the velocity and distance travelled can then be determined using a linear relationship. By utilizing this relationship in conjunction with a range of standardized wave speeds and possible crustal thicknesses, a line in thickness (‘H’), versus  $V_p/V_s$  ratio (‘k’), space can be determined for each conversion arrival (see Fig. 2). When the linear relationships between all three arrivals for each earthquake are combined, the point of intersection indicates the unique solution to the three lines; this represents the best-fit thickness and wave-speed for the crust below that station.

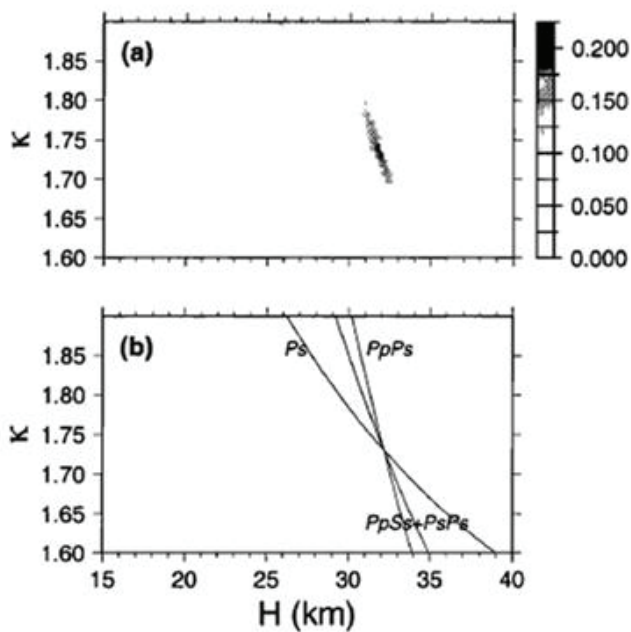


Fig 2. Taken from Zhu and Kanamori (5), this image shows how a single seismic event can be used to pinpoint a best-fit estimate of crustal thickness below the receiver using the relationship between the speed of the wave, the distance it travels, and how fast it travels that distance.

Many earthquakes were used simultaneously for each station by employing a script created by Helffrich (6) to stack all of

the RFs. This script uses standard vales - depths between 20 km and 50 km, velocity ratios between 1.5 and 2.0, and an assumed P-wave velocity of 6.5 km/s. Because this method compares arrivals of the P-wave coda to the initial P-wave arrival it is robust to different P-wave velocities, meaning that the results should not vary greatly for different assumed P-wave speeds. According to Zhu and Kanamori (5), the estimates provided are sufficiently accurate for approximately a 10 km radius cone beneath the station.

Only large teleseismic earthquakes, meaning earthquakes that occurred between 30 and 90 degrees from an average location between all of the stations (49.859689, -75.223378) with magnitude greater than 6.0, were used for this study. The magnitude had to be adequately high in order to ensure a large signal to noise ratio, as shown in Fig. 3. The spatial constraints on this search were to ensure a steep incidence angle on the incoming ray path, which maximized incoming wave energy, allowed for the transmission of S-waves, and minimized disruptions due to lateral inconsistencies and vertical velocity contrasts.

The RF stacking code (6) was used on each station to identify a thickness estimate, all of which are compiled in Fig 4. Note that because NEMQ and NMSQ are in such close proximity to one another and do not overlap in time they were run as one station (NEMQ/NMSQ).

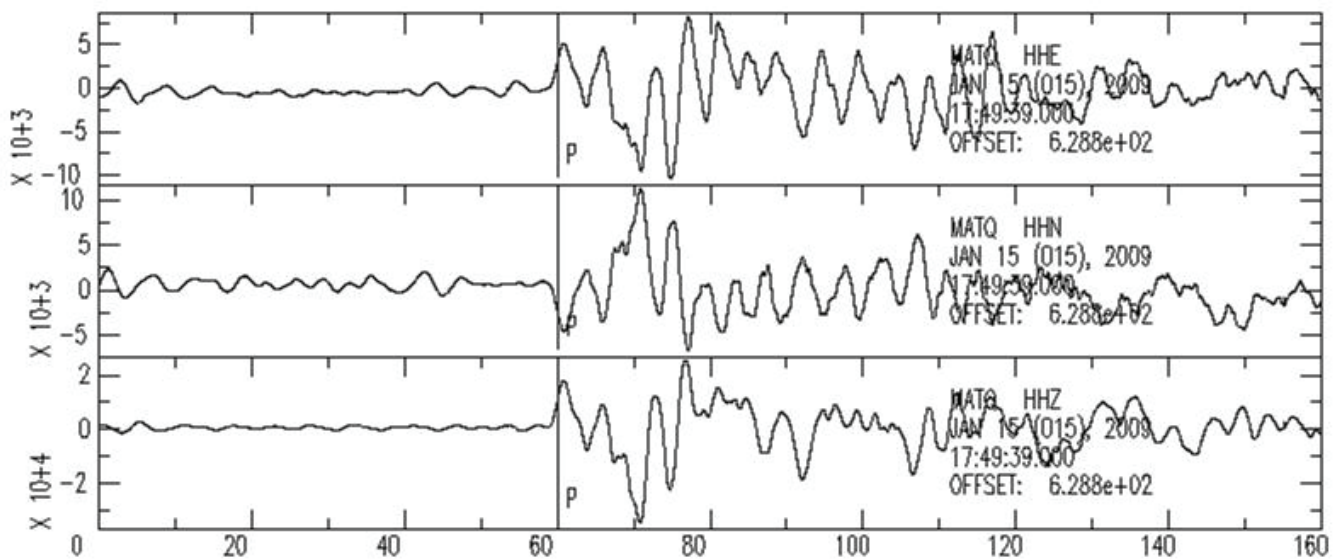


Fig 3. Sample of a "GOOD" seismogram from MATQ station (January 15th, 2009, at 5:49:39PM). A high signal to noise ratio makes identification of the incoming conversions easy to spot.

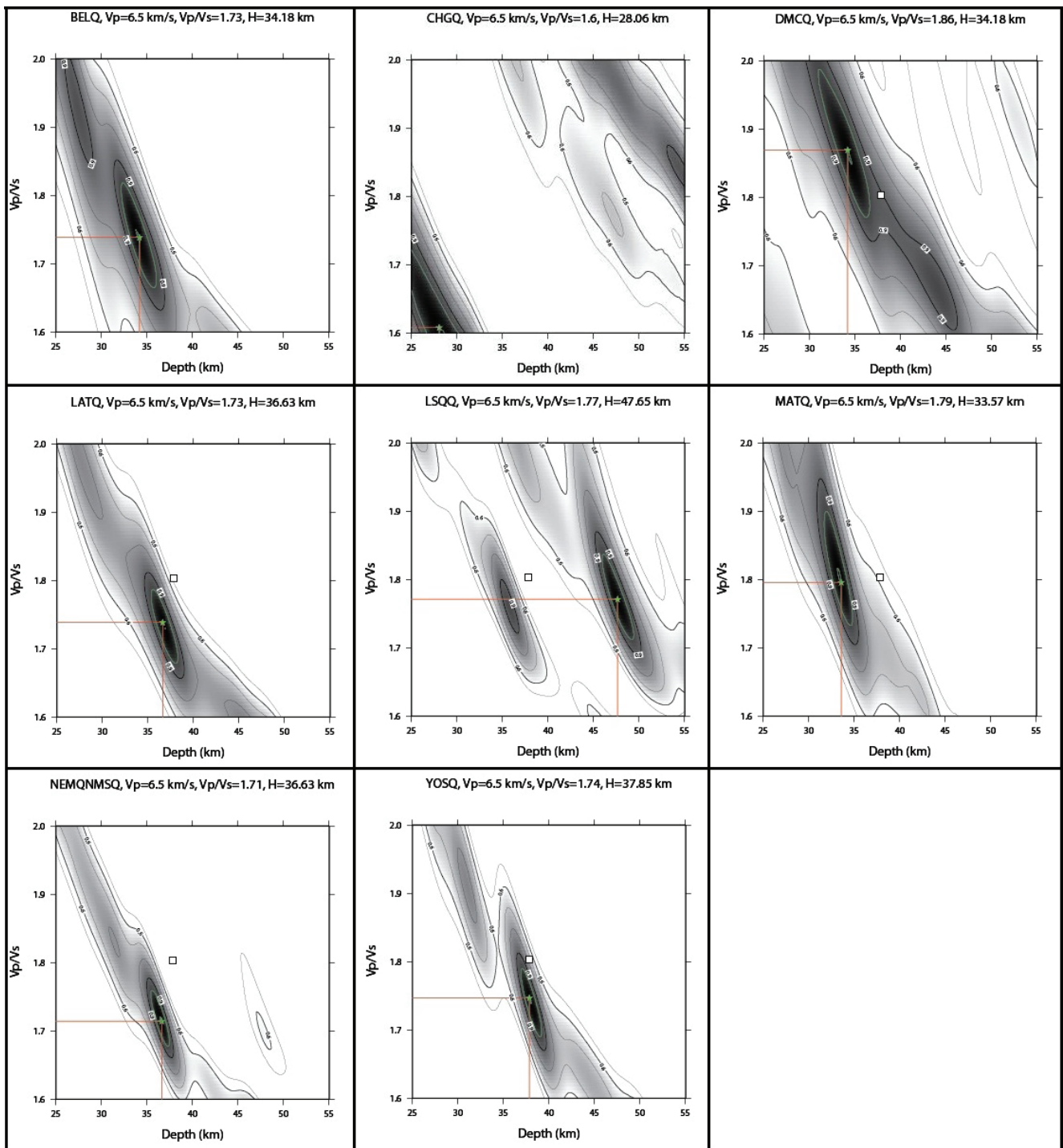


Fig 4. Plots created for each station using code by George Helffrich (6). Best-fit thickness identified for the stacked receiver functions.

## RESULTS

In order to test the validity of the RF stacking results they were compared to available previous estimates and to synthetic receiver functions created using code by Helffrich (6). These were prepared for several crustal parameters, including (but not limited to): thickness, Poisson's ratio, and slowness of rays. The Ps arrival times were calculated for receiver functions of synthetic seismograms arriving in crust with thickness ranging from 25 to 50 km, as shown on Fig 5. Five sample events were then taken from each station and Ps arrival time was manually identified. Using this arrival time and interpolating between the different synthetic arrival times, an estimate was made for the crustal thickness (Fig 6), which could be compared directly to the value calculated using the RF stack. This comparison illustrates how well the actual station may fit with a simple 1D, homogenous, anisotropic crust.

The BELQ seismic station is located near Abi96 which used reflection seismology to measure a crustal depth of about 35 km (3). This is similar to the value obtained using receiver functions - a depth of 34.18 km (Fig 4). The synthetic estimate for thickness at this location was slightly lower, at 30 km.

CHGQ showed a very small thickness value of 28.06 km in RF stack (Fig 4). It seems that a more thorough investigation of this area might render slightly different results, given that the expected values from the LITHOPROBE lines are between 35 and 40 km (2), and the synthetic estimate predicts a value closer to 34 km.

The DMCQ thickness estimate of 34.18 km (Fig 4) is less than predicted by both previous work and synthetics, given the estimates made by Ludden and Hynes (2). They anticipated a thickness of the crust in the western Grenville province to be between 40 and 45 km, while the synthetic receiver functions indicated a 39 km thick crust (Fig 6). This particular station lies within an intrusion, which could be why it has such a high  $V_p/V_s$  ratio, 1.86, compared to that of LATQ, which also lies within the Central Granulite Terrain of the Grenville Province.

The RF stack value for thickness at La Tuque (LATQ) is 36.63 km (Fig 4), which corresponds well to the synthetic estimate of 36 km (Fig 6). This H-value is slightly lower than anticipated, based on the work of Ludden and Hynes (2), though not inconsistent with the estimates of Eaton et al (4). The  $V_p/V_s$  ratio, 1.73, is still high, though, as was suggested by the same paper.

Because LSQQ is located within the Abitibi Greenstone Belt thickness was expected between 35 and 40km (3). The calculated value, 47.65 km (Fig 4), is much thicker. However, there appears to be two areas of best-fit on the plot with similar  $V_p/V_s$

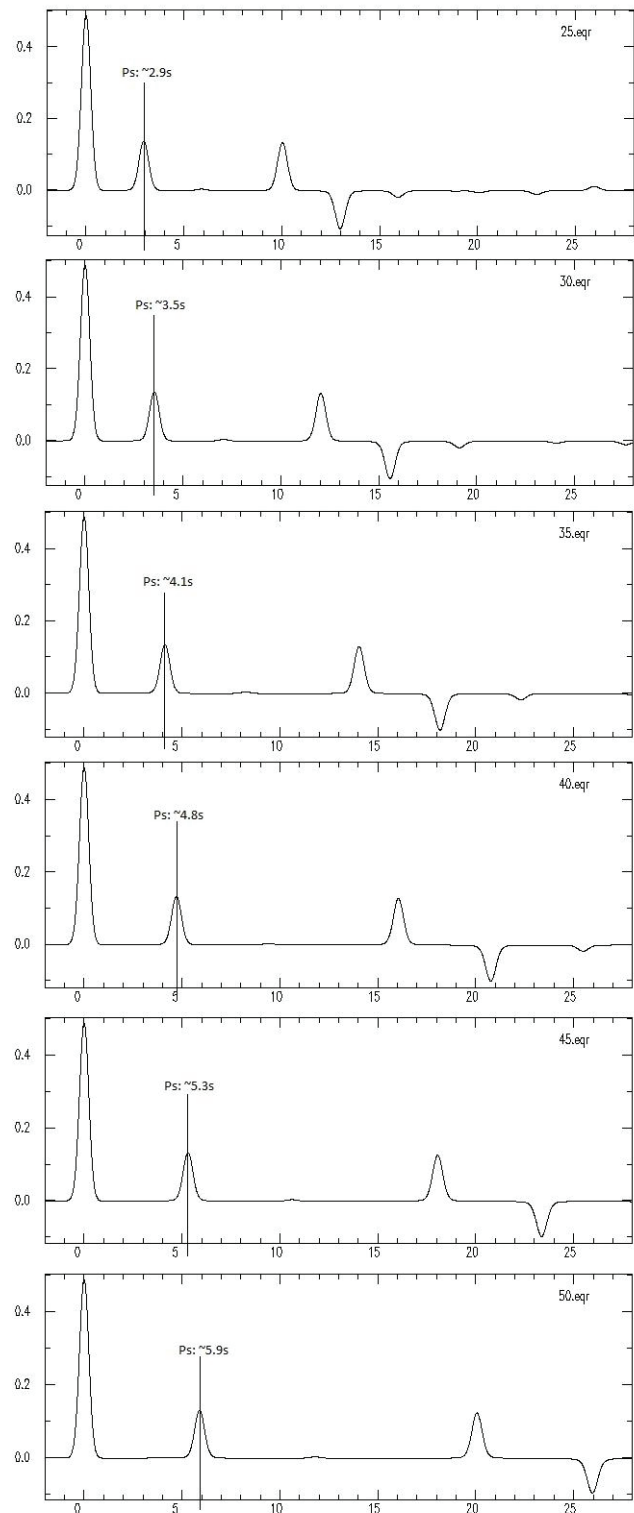


**Fig 5.** Synthetic receiver functions created for different crustal thicknesses to simply model how arrival time varies with crustal thickness. 25 km: 2.9 s, 30 km: 3.5 s, 35 km: 4.1 s, 40 km: 4.8 s, 45 km: 5.3 s, 50 km: 5.9 s.

Station Name	Avg Ps arrival for 5 samples (s)	Corresponding Synthetic Thickness (km)	Expected Arrival Time (s)	Stacked Thickness Estimate (km)
BELQ	3.5	30	3.98	34
CHGQ	4.02	34	3.26	28
DMCQ	4.7	39	3.98	34
LATQ	4.27	36	4.38	37
LSQQ	4.38	37	5.66	48
MATQ	3.86	33	3.98	34
NEMQNMSQ	4.4	37	4.38	37
YOSQ	4.42	37	4.52	38

**Fig 6.** Table of values for thickness and Ps arrival time for each station. Synthetic Thickness is calculated by comparing PS arrival times of 5 sample events to the synthetically created RF's. Stacked Thickness was found using the Zhu and Kanamori (5) method.

Vs values. Upon consideration of the synthetic value (Fig 6), it is possible that the other solution, 36 km, fits better with the data set.

MATQ station is located near LITHOPROBE A-G transect 48 (2). It was suggested by Ludden that the transect contains a deep, inactive fault which remains from an ancient subduction zone and has an average crustal depth of about 35km. This corresponds well to the values obtained in this study, of 33.57 km for the RF stack and 33 km for the syntheticsn (Figs 4 and 6, respectively).

The Opatoca Plutonic Belt – parts of which were interpreted by LITHOPROBE (2) – is believed to be a magmatic arc accreted onto the Superior Proto-Craton. It was then underthrust by the Abitibi, resulting in a broad, north-dipping synform in the crust. Similar to the results from MATQ, there may be relicts of an ancient subduction zone here. The values calculated for NEMQ/NMSQ, 36.63 km stacked and 37 km synthetically (Figs 4 and 6, respectively), match nicely with the range predicted by Ludden and Hynes (2).

Located within the understudied Superior Province, no estimate was available for YOSQ. The value calculated here, 37.85 km (Fig 4), therefore cannot be tested against previous work. However, it does match nicely with the synthetically estimated value of 37 km (Fig 6).

## DISCUSSION

The limitations of the receiver function stacking method are similar to those of the synthetic estimates. Both procedures assume that the crust of the earth can be modelled as a homogenous

1-dimensional layer sitting on top of the mantle. By placing one value to the entire crust, they negate the effect of anisotropic minerals, relic structures such as subduction zones and imbricate stacks, discontinuous layers, and all manner of heterogeneity. It is likely that in the future more detailed models which account for layers with velocity contrasts will yield more accurate results. In the interim, it is possible to make some preliminary conjectures about the depth to the crust-mantle boundary in southern-central Quebec.

For many stations, there is an approximate correlation between previous studies, stacked values, and synthetically modelled estimates. It is reasonable to assume that this means that the structure below these stations – Belleterre, La Tuque, Matagami, and Nemaska/Némiscau– is fairly uniform and lacks strong vertical structures. In stations such as CHGQ, DMCQ, LSQQ, and YOSQ we see secondary peaks in the RF stacks, which most likely indicate dipping structures. This hypothesis could be tested in future studies by breaking down analysis by back-azimuth to see if thicker and thinner estimates are coming from opposite sides of the station. For locations, such as Dolbeau and Lebel-sur-Quévillon with their anomalously high thickness estimates, further work must be done and additional data obtained to confidently ascertain the crustal thickness.

CHGQ presents the most indeterminate result of all. Upon closer inspection of the later phases, PpPs, PsPs, and PpSs, it is evident that the arrival time varies drastically as a function of incoming direction (back-azimuth). This may be the result of a lateral heterogeneity in the crust, multiple layers, or a steeply dipping structure below Chibougamau. Nonetheless, it is evident that simple 1D modelling of this area will not yield relevant and acceptable results, despite the tempting match between the synthetic estimation and LITHOPROBE results (2). Further

studies into the anisotropy of the area may help characterise this idiosyncrasy.

The  $V_p/V_s$  ratios can be used to identify the general composition of the crust beneath the stations. While it may seem that the majority of the crust would be polarized between a predominantly felsic bulk composition and the mafic Abitibi greenstone, we see that there is a broad distribution ranging between 1.6, which is very felsic, and 1.86 which is relatively more mafic. The highest value, 1.86, was not found in the Abitibi at all, whereas the 1.6 value was. This suggests that either the  $V_p/V_s$  ratio is affected by more than just mafic/felsic composition, or our  $V_p/V_s$  estimations are not accurate enough at this time to fully predict the behaviour that we can observe through field observations.

## CONCLUSION

This study estimated the Moho depth at 9 seismic stations in Southern and Central Quebec. Overall the values obtained here match with both previous estimates and synthetically generated seismograms, varying between about 28 and 48km. There were problems in matching at stations where either enough data was not available at the time of study, or complicated deep crustal structures preclude model accuracy. For these sites – CHGQ and LSQQ – future work may reveal dipping structures or heterogeneities within the crust.

## REFERENCES

1. F. A. Darbyshire, D. W. Eaton, A. W. Frederiksen, L. Ertolahti, *Geophys J Int* **169**, 1043 (2007).
2. J. Ludden, A. Hynes, *Can J Earth Sci* **37**, 459 (2000).
3. S. Rondenay *et al.*, *Can J Earth Sci* **37**, 415 (2000).
4. D. W. Eaton, S. Dineva, R. Mereu, *Tectonophysics* **420**, 223 (2006).
5. L. Zhu, H. Kanamori, *J Geophys Res* **105**, 2969 (2000).
6. G. Helffrich, *Bull Seismol Soc Am* **96**, 344 (2006).

# Bayesian Models for Phylogenetic Trees

Clarence Leung\*<sup>1</sup>

<sup>1</sup>McGill Centre for Bioinformatics, McGill University, Montreal, Quebec, Canada

## ABSTRACT

**Introduction:** Inferring genetic ancestry of different species is a current challenge in phylogenetics because of the immense raw biological data to be analyzed. Computational techniques are necessary in order to parse and analyze all of such data in an efficient but accurate way, with many algorithms based on statistical principles designed to provide a best estimate of a phylogenetic topology. **Methods:** In this study, we analyzed a class of algorithms known as Markov chain Monte Carlo (MCMC) algorithms, which uses Bayesian statistics on a biological model, and simulates the most likely evolutionary history through continuous random sampling. We combined this method with a Python-based implementation on both artificially generated and actual sets of genetic data from the UCSC Genome Browser. **Results and Discussion:** We observe that MCMC methods provide a strong alternative to the more computationally intense likelihood algorithms and statistically weaker parsimony algorithms. Given enough time, the MCMC algorithms will generate a phylogenetic tree that eventually converges to the most probable configuration.

---

\*Corresponding author:  
clarence.leung@mail.mcgill.ca  
Received: 2 January 2012  
Revised: 2 March 2012

## INTRODUCTION

### GENETICS AND PHYLOGENY

The rise of genetics in the past few decades has led to a significant shift in the techniques and primary focuses of biological research. Quantitative data analysis has begun to replace the purely observational techniques used in the past, and new fields of study have sprouted in response to considerable data that we have yet to analyze and apply (11).

Phylogenetics, the study of the evolutionary relatedness between organisms, has been one such field bombarded by an influx of raw data. From the study of taxonomy, the identification and classification of organisms, phylogenetics research has merged quantitative data and gene inheritance theories into the development of past evolutionary inferences. The techniques used in phylogenetic analysis range from computing evolutionary distances between two individual organisms, to estimating divergence times between species, to even analyzing diversification rates of all life at the macroscopic level (6).



Fig 1. A sample DNA dataset represented in digital format. Source: Wikimedia Commons

The phylogenetic tree is an intuitive way of representing these phylogenetic relationships, and has long been used by researchers to model the unique genetic characteristics of each individual species. Topologically, a phylogenetic tree is composed of two groups of sub-structures, nodes and branches. The nodes of a phylogenetic tree can represent any unit of phylogeny, ranging from a single gene to an entire taxon of organisms (3, 8). Similarly, the branches of a tree can represent any method of describing the differences between any two units, at the genetic level (such as the Hamming distance between any two DNA sequences) or even time (10). Though phylogenetic trees have historically been used to model taxonomy because they are similar to the actual evolutionary patterns of adaptive radiation and lineage splitting, phylogenetic trees in today's studies have been used as more dynamic models to demonstrate the specific processes, such as nucleotide mutation, that lead to those macroscopic changes (2).

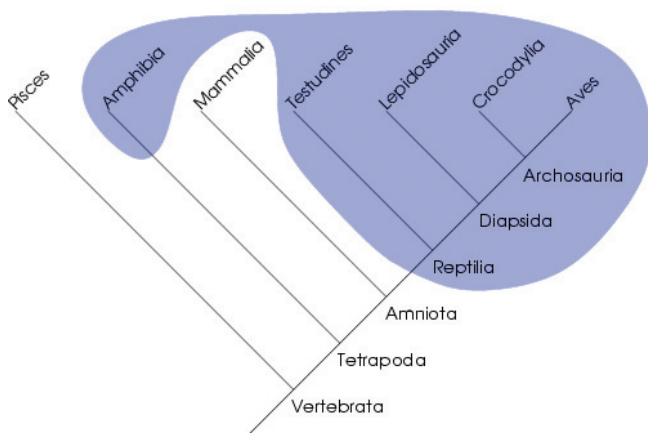


Fig 2. A rooted phylogenetic tree for sample rRNA genes, showing the branches Bacteria, Archaea, and Eucaryote. Source: Wikimedia Commons

In recent years, phylogenetic inferences have begun to rely increasingly on large amounts of molecular data sets, such as the sequences of DNA or amino acids because of the growing ease and reduced costs of obtaining sequence data due to more efficient sequencing techniques (5). As more and more quantitative data is gathered in various fields, phylogeneticists must analyze and process that data to modify their predictions of evolutionary relationships.

**COMPUTATIONAL PHYLOGENETICS**

Computational methods are necessary to investigate these sequence datasets, as their sheer size make manual data analysis nearly impossible. Algorithmic methods of solving phylogenetic problems have been developed to solve these problems in a feasible computational time and compute significant results including phylogenetic tree inferences. Though there are many types of algorithms used in phylogenetics, they all rely on the use of computational statistics in order to generate predictions of the evolutionary past, given the molecular sequences of modern day organisms.

Algorithms in phylogenetic tree inference will take as input molecular sequences of modern-day organisms, and set them as the external nodes of the tree, or the nodes that do not have child nodes below it. Through different calculation methods, these algorithms generate statistical phylogenetic predictions of the desired genetic information of the parent nodes and the branches between each node, working up through the tree until the root is reached. The final output of the algorithm is a completed phylogenetic tree, with the most likely inferences for the node and branch parameters solved. These algorithms can be divided into one of three main types, classified by their method of calculation (2, 6, 9).

**MAXIMUM PARSIMONY:**

Using this class of algorithms, the most likely phylogenetic tree is the one that has the least evolutionary change that results in the observed data. Each sub-tree of the phylogenetic tree is scored by a scoring mechanism, which is determined by the number of steps required to change from a parent node to a child node, for each node in the sub-tree. These algorithms are simple, but often inconsistent, as adding more data to a calculated tree will sometimes lead to a completely different tree, rather than converging on the same result.

**MAXIMUM LIKELIHOOD:**

Under this class of algorithms, the sequence data of a specific sub-tree is scored, and the scoring function works up the tree. However, instead of scoring with a function that calculates the least amount of change, the transition probability of that character changing at any point in the sub-tree is calculated by a specific probability model based on the character of each sequence, such as a single nucleotide or amino acid. Scoring is based on the combined likelihoods determined by the function, and produces a much more likely tree than parsimony. However, these algorithms tend to be extremely computationally intensive, especially as the number of parameters accepted by the probability model increases.

**BAYESIAN INFERENCE:**

Under this class of algorithms, the same character transition probability model is used, as in maximum likelihood. However, rather than determining the tree heuristically with a scoring function, as in maximum likelihood, Bayesian algorithms run continuous simulations of generating evolutionary trees through Markov chain Monte Carlo (MCMC) algorithms. These trees are randomly generated with probability based on a given density, and are based upon Bayes' theorem, which determines the conditional probability of a specific tree given existing data. These algorithms are faster and more efficient than other algorithms, and are able to accept many different parameters while generating converging trees.

**MARKOV CHAIN MONTE CARLO ALGORITHMS**

We want to calculate the probability of a specific tree given the current data. By Bayes' theorem, we note this as:

$$P(T|D) = P(T) \cdot \frac{P(D|T)}{P(D)}$$

Where  $P(T|D)$  represents the probability of the tree, given the data,  $P(T)$  represents the overall probability of the tree, and  $P(D|T)/P(D)$  the effect of  $T$  on the probability of  $D$ . In Bayesian inference, these are the posterior distribution, the prior distribution, and the likelihood, respectively. These probabilities are simple to calculate with discrete probabilities, but difficult to

calculate with biological probability models, which require multi-dimensional integrals that can combine both continuous and discrete calculations.

Instead of directly sampling from the complex distribution, A possible solution is to construct a Markov chain, a chain system that transitions from one state to another while satisfying the Markov property, where the probability of the next state of the system is dependent only on the current state of the system. Formally, we define a Markov chain as:

$$P(X_{n+1} = x | X_1 = x_1, X_2 = x_2, \dots, X_n = x_n) = P(X_{n+1} = x | X_n = x_n).$$

Where all of the possible probabilities of the Markov chain  $\{x_1, x_2, \dots, x_n\}$  are known as its space.

To sample from a complex distribution, a Markov chain of probability distributions can be created such that its equilibrium state, where the Markov chain converges to some steady state, will be equivalent to that complex distribution. Thus, the correctness of the MCMC sampler will improve after each iteration of the Markov chain, and the probability distribution will be closer to the actual distribution we are trying to sample. Generating the Markov chain is not difficult, as we can start from any given distribution, and adjust it depending on the given density function at each iteration.

However, determining when an MCMC sampler has converged is more difficult because the randomness of the algorithm could potentially generate several states without having actually made any changes, but not be equivalent to the target distribution.

**METROPOLIS-HASTINGS SAMPLER**

A specific version of the MCMC sampler for probability distributions is the Metropolis-Hastings sampler, which allows sampling from any probability distribution if a function proportional to the corresponding probability density is known. For some complex distribution  $\Pi(x)$  and its corresponding density  $\pi(x)$ , and some transition proposal distribution  $Q(x, y)$  and its density  $q(x, y)$ , if we are currently at state  $x$  in the chain, we select a draw for a candidate state  $y$  from  $Q(x, \cdot)$  with probability  $\alpha(x)$  given by:

$$\alpha(x, y) = \min \left\{ \frac{\pi(y)q(y, x)}{\pi(x)q(x, y)}, 1 \right\}$$

Note that  $\pi(y)/\pi(x)$  is the likelihood ratio between the current state and the next state, and  $q(y,x)/q(x,y)$  is the ratio of the proposal density in two directions to adjust for density skewness. If the density is symmetric, then the ratio of the proposal density in the two directions is 1, which reduces our algorithm to only be dependent on the likelihood ratio, and converts it into a

Metropolis sampler, a subclass of the generalized Metropolis-Hastings algorithm.

If the combined probability  $\pi(y)q(y,x)/\pi(x)q(x,y)$  is greater than 1, then the draw is automatically accepted, and the Markov chain will now be in state  $y$ . Otherwise, we transition to state  $y$  with that probability, so there is a possibility that we reject the draw and remain in our current state with probability  $1 - \pi(y)q(y,x)/\pi(x)q(x,y)$ .

## BAYESIAN INFERENCE IN PHYLOGENETICS

In MCMC algorithms acting on phylogenetic trees, a Metropolis-Hastings sampler can be created where  $\pi(x)$  will be the conditional density of the candidate phylogenetic tree, given the observable character sequences (3). The proposal density  $q(x)$  will modify the topology of the branches of the tree that has been affected, and the character sequences of any nodes of the tree that have been affected. The density  $q(x)$  will be dependent on a character transition model that takes into account outside parameters that can include time, character transition ratios, and rates of transition (4). We describe an example of such a model in the following section for a series of nucleotide sequences where nucleotide mutation is determined by the Hasegawa, Kishino, and Yano (1985) nucleotide transition model, and describe an implementation (8).

## DESCRIPTION OF THE MODEL

### NUCLEOTIDE TRANSITION MATRIX

The Hasegawa, Kishino, and Yano (HKY85) nucleotide transition model allows for the consideration of five parameters: the four base frequencies of the possible nucleotides adenine, thymine, cytosine, and guanine, denoted as  $\pi_A, \pi_T, \pi_C, \pi_G$  and a transition/transversion rate parameter  $\kappa$  that allows for the differentiation between the transitions of purines (A, G) and transitions of pyrimidines (C, T).

This can be expressed in the rate matrix  $Q$ :

$$Q = \begin{pmatrix} * & \kappa\pi_C & \pi_A & \pi_G \\ \kappa\pi_T & * & \pi_A & \pi_G \\ \pi_T & \pi_C & * & \kappa\pi_G \\ \pi_T & \pi_C & \kappa\pi_A & * \end{pmatrix}$$

The transition probability for some time  $t$  and nucleotide transition  $I$  to  $j$ ,  $Q_{ij}(t)$ , can then be described as:

$$Q_{ij}(t) = \begin{cases} \pi_j + \pi_j \left( \frac{1}{\lambda_j} - 1 \right) e^{-\alpha t} + \left( \frac{\lambda_j - \pi_j}{\lambda_j} \right) e^{-\alpha \gamma_j t} & \text{if } i = j \\ \pi_j + \pi_j \left( \frac{1}{\lambda_j} - 1 \right) e^{-\alpha t} + \left( \frac{\pi_j}{\lambda_j} \right) e^{-\alpha \gamma_j t} & \text{if } i \neq j, \text{ transitional event} \\ \pi_j (1 - e^{-\alpha t}) & \text{if } i \neq j, \text{ transversional event} \end{cases}$$

Where  $\alpha$  is some normalizing constant that allows all probabilities to sum to 1,  $\lambda_j = \pi_A + \pi_G$  if  $j$  is a purine (A or G) or  $\lambda_j = \pi_C + \pi_T$  if  $j$  is a pyrimidine (C or T), and  $\gamma_j = 1 + (\kappa - 1)\lambda_j$ .

## METROPOLIS-HASTING ON TREES

We draw a potential state for the next tree in the Markov chain with an algorithmic method in four steps:

### 1. REARRANGE THE LOCAL TOPOLOGY

A random internal node that has both a parent and children is chosen, which is designated our target node  $T$ . We now rearrange the local topology of the node, which consists of the neighboring nodes  $C1, C2$ , and  $S$ , representing the first child, the second child, and the sibling of the target node respectively. A new topology is chosen by randomly rearranging the positions of those nodes, and their subtrees as well.

### 2. SELECT A NEW TARGET TIME

Using the new topology, a new time for the target is selected by choosing from the density:

For  $\max\{t_{C1'}, t_{C2'}\} \leq t_{T'} \leq t_P$ :

$$g(t_{T'}) = \frac{\sum_{v \in D^m} P_{v_P v}(t_P - t_{T'}) P_{v v_{C1'}}(t_{T'} - t_{C1'}) P_{v v_{C2'}}(t_{T'} - t_{C2'})}{\int_{\max\{t_{C1'}, t_{C2'}\}}^{t_P} \sum_{v \in D^m} P_{v_P v}(t_P - t_{T'}) P_{v v_{C1'}}(t_{T'} - t_{C1'}) P_{v v_{C2'}}(t_{T'} - t_{C2'})}$$

Note that the selected time of the target node must fall between the time of the parent node, given by  $t_P$  and the time of its nearest child, given by  $\max\{t_{C1'}, t_{C2'}\}$ , after the nodes have had their topology rearranged.

When calculating this time, we do not actually have to sum all  $4^m$  different nucleotide sequences when implementing the selection. Because the nucleotide sequences of the parents and the descendants in the summation are always fixed, we actually will only need to evaluate  $4^3 = 64$  total terms per iteration, which significantly increases the algorithm's speed.

### 3. SELECT A NEW TARGET SEQUENCE

When determining the nucleotide sequence, this density can be simplified to a series of four-nucleotide draws, with frequencies dependent on a four-category multinomial distribution that is recalculated at each iteration. We can sample individually from a categorical distribution for each nucleotide in the sequence, as the probability of a mutation for each nucleotide is not dependent on any other states in the current iteration.

For  $v_{T'} \in D^m$ :

$$h(t_{T'}) = \frac{P_{v_P v_{T'}}(t_P - t_{T'}) P_{v_{T'} v_{C1'}}(t_{T'} - t_{C1'}) P_{v_{T'} v_{C2'}}(t_{T'} - t_{C2'})}{\sum_{v \in D^m} P_{v_P v}(t_P - t_{T'}) P_{v v_{C1'}}(t_{T'} - t_{C1'}) P_{v v_{C2'}}(t_{T'} - t_{C2'})}$$

#### 4. ACCEPTANCE OR REJECTION OF THE CANDIDATE

After selecting this candidate state, the algorithm must decide whether or not it is accepted as the next state in the chain or rejected.

$$\alpha(x, y) = \min \left( \frac{\int_{\max(t_{C1}, t_{C2})}^{t_P} \sum_{v \in D^m} P_{vPv}(t_P - t) P_{vvc_1'}(t - t_{C1'}) P_{vvc_2'}(t - t_{C2'}) dt}{\int_{\max(t_{C1}, t_{C2})}^{t_P} \sum_{v \in D^m} P_{vPv}(t_P - t) P_{vvc_1}(t - t_{C1}) P_{vvc_2}(t - t_{C2}) dt} \frac{P_{vPvS}(t_P - t_S)(n_T + 1)}{P_{vPvS}(t_P - t_S)(n_T + 1)}, 1 \right)$$

This is the  $\alpha(x, y)$  as noted before in the MCMC algorithm, the combination of the target distribution and the proposal density. If the probability of selection is greater than or equal to 1, then we automatically select the new state, with the new topology, time, and sequence. Otherwise, we will move to the new state with probability  $\alpha$ , and stay at our current state (reject the candidate) with probability  $1 - \alpha$ .

## EXPERIMENTAL DATA

We compared the MCMC algorithm with several known techniques in computational phylogenetics, as described above. An implementation of the MCMC algorithm was created in the Python programming language, with the NumPy and SciPy scientific computing libraries, and compared against the non-Bayesian algorithms found inside the PHYLIP phylogenetic inference package, written in C. The Python MCMC algorithm had its results validated with MrBayes, a generalized MCMC phylogenetic inference package written in R.

Three alternate algorithms were chosen from the PHYLIP package to demonstrate the variety of methods available to calculate the most likely phylogenetic tree:

##### 1. DNAPARS

A maximum parsimony algorithm based on several improvements to the Fitch algorithm (1971).

##### 2. DNAPENNY

A maximum parsimony algorithm using the "branch and bound" method devised by Hendy and Penny (1982).

##### 3. DNAML

A maximum likelihood algorithm based on an algorithm devised by Felsenstein (1981) and a model by Hasegawa et al. (1985).

## ARTIFICIALLY GENERATED DATA

The algorithm was initially tested on a small artificially generated dataset obtained from the PHYLIP phylogenetic inference package. This dataset is designed to test the accuracy of phylogenetic algorithms through simulations of nucleotide mutation starting from a chosen root sequence.

Sequence Label	Nucleotide Sequence
Alpha	AACGTGGCCACAT
Beta	AAGGTGCGCCACAC
Gamma	CAGTTCGCCACAA
Delta	GAGATTTCCGCCT
Epsilon	CTGATGTCCGCAT
Zeta	CAGATGGCCACAT
Eta	GAGATGGCCGCAT
Theta	CTGTTGCGCCACCT

Fig 3. The small artificial dataset used to test the validity of the algorithm.

The algorithms were capable of producing trees with similar topologies, although some tree rearrangement is required. We repeated this method multiple times with several different bootstrapped versions of the initial topology, using PHYLIP's BOOTSTRAP program to generate a new shuffling of DNA sequences. Using the CONSENSE program in PHYLIP, we built a consensus tree for each different algorithm type, with a chain of 500 trees for the MCMC algorithm, and 500 random trees starting from the bootstrapped topologies for the rest.

The ratios on the intersections of each branch represent the number of trees sampled that contained that specific "majority" sub-tree. In particular, if 0.99 is the ratio on the intersection, then 0.99 of all trees sampled would contain that specific sub-tree on the branch.

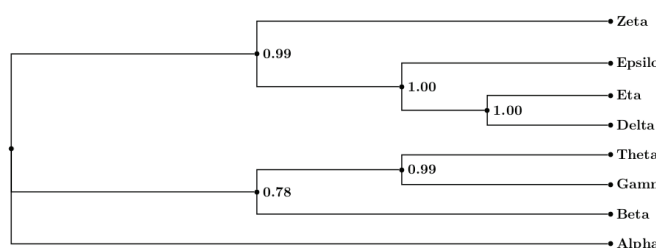
## UCSC GENOME BROWSER DATA

After validating the data with the artificial dataset, actual sequence data from the UCSC Genome Browser was used to determine the applicability of the MCMC algorithm on a larger dataset, based on experimentally-obtained sequence alignments. A 896-nucleotide strand from the MT-ND4 (mitochondrially encoded NADH dehydrogenase 4) gene on human alignment hg19 was taken and compared with similar regions found in several other primate species such as the tarsier (with alignment tarSyr1), the gorilla (with alignment gorGor3), and the orangutan (with alignment ponAbe2).

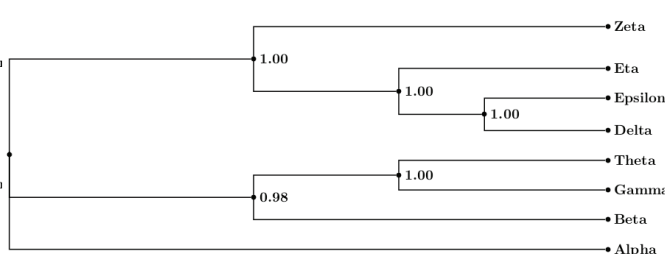
After calculating our first optimal tree, we determined the consensus tree for each algorithm using the same method as before.

The average ratios for the subtrees of each method were 0.84 for maximum parsimony, 0.88 for branch and bound, 0.98 for maximum likelihood, and 0.93 for MCMC.

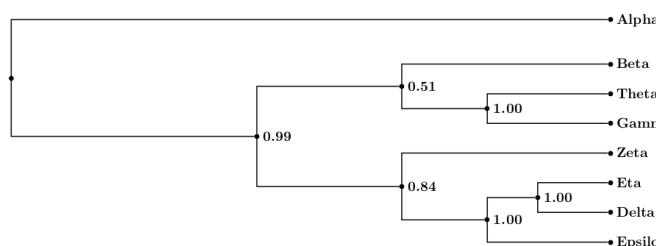
3.2.1 Maximum parsimony



3.2.3 Maximum likelihood



3.2.2 Maximum parsimony (Branch and bound)



3.2.4 Markov chain Monte Carlo

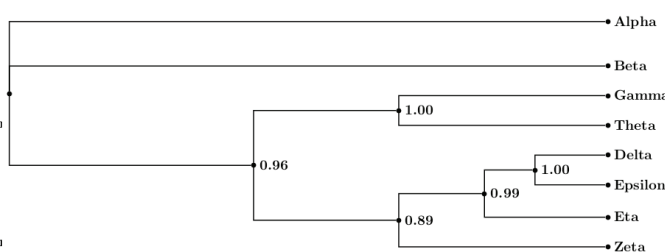
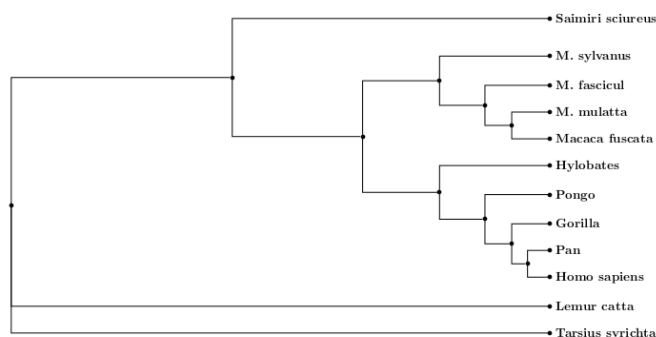
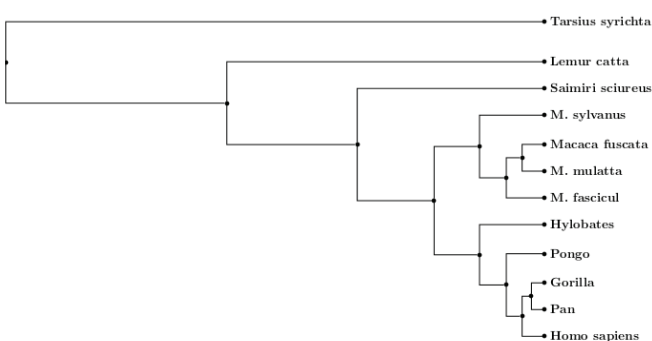


Fig 4. The resulting consensus trees for the different algorithms on the artificial dataset.

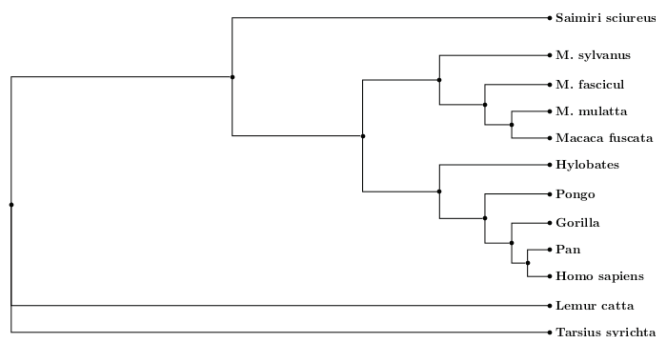
3.3.1 Maximum parsimony



3.4.1 Maximum likelihood



3.4 Maximum parsimony (branch and bound)



3.4.2 Markov chain Monte Carlo

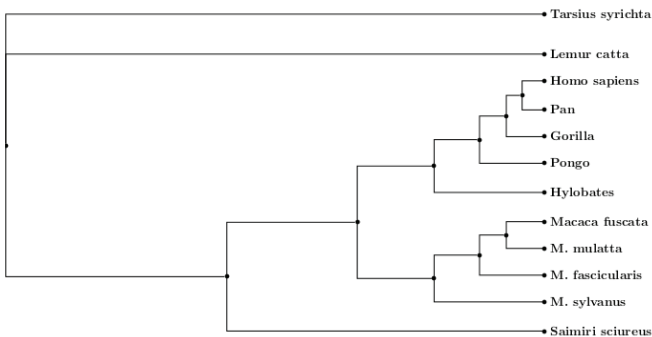


Fig 5. The resulting consensus trees for the different algorithms on the UCSC Genome Browser dataset.

## DISCUSSION

### COMPARISON WITH OTHER ALGORITHMS

The MCMC algorithm performed well with respect to accuracy and efficiency in each of the cases we considered, both on the artificial sample dataset and actual genetic data obtained from the UCSC Genome Browser. However, the implementation of this specific algorithm was slower than established algorithms because it was developed in the Python programming language for rapid development, rather than the C programming language for computational efficiency, as were the maximum likelihood and maximum parsimony algorithms. However, in comparison with an R implementation of the MCMC algorithm in MRBAYES, the maximum likelihood algorithm took significantly more computational power and more time in order to determine the final phylogenetic tree.

From the consensus tree, the algorithms based upon Bayesian statistical models (the MCMC and maximum likelihood algorithms) generated phylogenetic trees that were more similar to each other than to ones generated by the parsimony algorithms. This is an expected outcome, as maximum parsimony is known to statistically deviate from similar but slightly different conditions. Felsenstein (1978) showed that maximum parsimony algorithms will often result in significantly different outcomes if there is a scenario under long-branch attraction scenarios, which tend to occur with rapidly evolving species (4). Although Bayesian methods use probabilistic algorithms and will have more random initial phylogenetic trees, the ability for probability distributions to converge will in fact result in more stable sets of trees. However, these methods rely on having a correct stochastic model for the transition probabilities of each character (be it a nucleotide or an amino acid). Many parameters must be taken into consideration in the construction of these stochastic models, and a model with false or incomplete assumptions can create a chain of improper trees.

### PYTHON FOR BIOINFORMATICS

The Python programming language, with scientific computing libraries NumPy and SciPy, were used to implement our algorithm. Unlike the more typically used low-level programming languages for bioinformatics such as C or Fortran, or those with powerful statistical libraries such as R, Python allowed for much more rapid development and prototyping of the algorithm, with many low level memory issues being abstracted by the Python interpreter. NumPy and SciPy, however, provided fast vectorization and many probability functions, many of which were wrappers for existing C or Fortran functions, which overcame some of the expected trade-off of algorithm speed for development time.

### FUTURE WORK

Phylogenetics remains a significant field in both the biological sciences and computing. As biological data becomes more widely available with the development of new experimental biology

techniques, modeling of DNA and proteins will become more precise as more prior parameters can be considered for the statistical model. Current research (1, 6) includes the application of population-level parameters beyond molecular-level parameters in the creation of the MCMC model, which has seen limited success. The difficulty now lies in the complexity of population-level parameters, some of which cannot be easily quantified. Environmental-level parameters will be the next step, but until researchers have the computational power to simulate an entire environment, this is not possible.

In addition to taking more parameters, MCMC algorithms should also be able to output more phylogenetic data than just the predicted ancestral sequences and times. Other studies have shown that extended MCMC algorithms can even assist in taxonomic classification, by helping to calculating taxonomic circumscription limits (2). These MCMC algorithms not only produce sequence data, but provide possible limits for species categorization. In the future, MCMC algorithms may create a new species classification system, based on genetics, as the Linnaeus system of classifying species by only their physical characteristics is outdated.

## ACKNOWLEDGEMENTS

I would like to show my gratitude to Professor Russell Steele for his guidance in this project, and especially for the creators of the open source software packages that were used in this study.

## REFERENCES

1. B. Arbogast, S. Edwards, J. Wakely, J. Slowinski, *Annu Rev Ecol Syst* **33**,707-740 (2002)
2. N. Bell, J. Hyvonen, *Am J Bot* **97**, 566-578 (2010)
3. H. Fan, L. Kubatko, *Mol Phy and Evo* **59**, 354-363 (2011)
4. J. Felsenstein, *Syst Zool* **27**, 401-410 (1978)
5. P. Green, *Biometrika* **82**, 711-732 (1995)
6. J. Hey, R. Nielsen, *P Natl Acad Sci USA* **104**, 2785-2790 (2006)
7. D. Husmeier, G. McGuire, *Bioinformatics* **18**, Sup 1 (2002)
8. S. Li, D. Pearl, H. Doss, *J Am Stat Assoc* **95**, 493-508 (1996)
9. B. Mau, M. Newton, B. Larget, *Biometrics* **55**, 1-12 (1999)
10. B. Rannala, Z. Yang, *Genetics* **164**, 1645-1656 (2003)
11. F. Ronquist, A. Deans, *Annu Rev Entomol* **55**, 189-206 (2010)
12. A. Siepel, D. Haussler, *J Comp Bio* **11**, 413-428 (2004)
13. Z. Yang, B. Rannala, *Mol Bio and Evo* **14**, 717-724 (1997)

# An Analytical Method Development for the Study of Chemical Species of Mercury in the Atmosphere

Ningsi Mei\*<sup>1</sup>

<sup>1</sup>Department of Chemistry, McGill University, Montreal, Quebec, Canada

## ABSTRACT

**Introduction:** Both natural and anthropogenic activities add mercury (Hg) to the atmosphere. The speciation and chemical transformation of mercury in the atmosphere can significantly influence how it is deposited on the Earth's surface. **Methods:** To better understand the impact of urban emissions on global mercury cycling, we developed an inexpensive technique for the reliable measurement of gaseous oxidized mercury (GOM) in air. This simple technique is based on a thermal decomposition-difference method previously developed by others for aircraft studies of GOM in the remote troposphere. Measurements of total atmospheric mercury (TAM) were made by decomposing all forms of mercury in ambient air to gaseous elemental mercury (GEM) at 500°C prior to detection using cold vapour atomic fluorescence spectroscopy (CVAFS). The amount of GOM was determined through the difference between TAM and GEM values.

**Results and Discussion:** A diurnal pattern was found for GEM, with the highest concentrations of Hg species found ranging from 2:00 to 5:00 PM and the lowest and most stable values from 9:00 PM to 6:00 AM. The amount of GOM was estimated on the 5<sup>th</sup> floor balcony of Pavillon Président-Kennedy at Université de Québec à Montréal to be  $14.7 \pm 10.3 \text{ ng}\cdot\text{m}^{-3}$  (arithmetic mean from eight groups of TAM-GEM differences in the afternoons of July 12 and 14, 2011 and 95% confidence interval). The inconsistent GOM result, in addition to a large error value, suggests the need for further investigation, and to compare the efficiency of this method to previously established methods to identify and quantify the mercury species in urban GOM.

## KEYWORDS

*Gaseous elemental mercury (GEM);  
Total atmospheric mercury (TAM);  
Mercury Speciation; Thermal decomposition;  
Gaseous oxidized mercury (GOM)  
measurements*

\*Corresponding author:  
ningsi.mei@mail.mcgill.ca  
Received: 3 January 2012  
Revised: 2 March 2012

## INTRODUCTION

Mercury is a toxic pollutant that poses danger to both humans and ecosystems. Bioaccumulation in the aquatic food chain and human body can potentially lead to serious health problems such as permanent brain damage (1, 2). Mercury participates in a number of complex environmental processes, best described as a series of chemical, biological and physical transformations. These govern the distribution of Hg in and between different compartments of the environment (3), which are illustrated in Fig. 1 (4). Both natural and anthropogenic (human) activities have been found to contribute to mercury emission to the atmosphere (5). While natural sources include volcanoes, soil, forests, lakes and open oceans, the anthropogenic sources are mainly industrial activities such as coal-burning power generation and municipal

and biomedical solid waste incineration (6). As the observed increase in Hg concentration following industrialization has been extensively documented (3), it is generally accepted that the anthropogenic emissions, concentrated in urban areas, have greatly increased relative to natural sources (6-7). There are several Hg species known to occur in the environment, three of which are most important (5). GEM [ $\text{Hg}^0$  or  $\text{Hg}(0)$ ] has a high vapor pressure and a relatively low solubility in water, making it the most stable atmospheric mercury species and subject to long-range transport. GOM (also referred to as reactive gaseous mercury or RGM) or divalent inorganic mercury [ $\text{Hg}^{2+}$  or  $\text{Hg}(\text{II})$ ] includes the mercury halides (e.g.  $\text{HgCl}_2$ ,  $\text{HgBr}_2$ , etc.). GOM is thought to be the principle form in wet deposition, as it has higher solubility than GEM and strong affinity for many inorganic and organic ligands. Particulate mercury (P-Hg) is the mercury bound to airborne particles whose lifetime in air is typically less than 10 days, though it depends on the size of the carrier particle. Elemental mercury vapor can circulate for up to a year, dispersing widely, during which a small portion may undergo photochemical oxidation to inorganic mercury. Inorganic mercury is easily scavenged by precipitation travelling to the Earth's surface. This mercury in rain is then deposited to soils and bodies of water. Once in soil or lake/river sediments, the mercury accumulates until a physical event causes it to be released again. Although  $\text{Hg}^0$  is the predominant form with only a few percent of the total present as GOM and Hg (8-9), GOM is particularly important because it can be readily scavenged by precipitation and has a much higher dry deposition velocity than  $\text{Hg}_0$  and P-Hg.

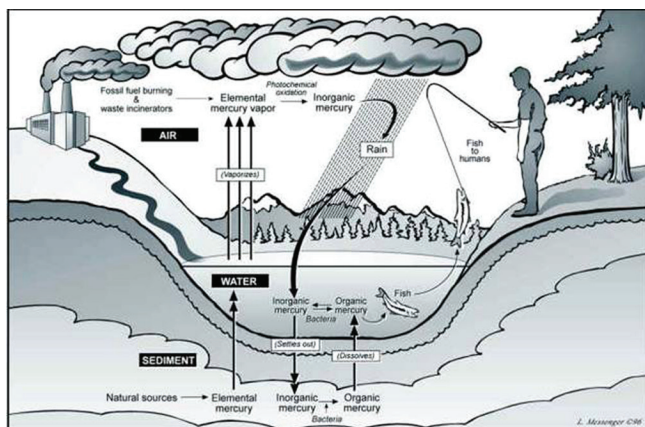


**Fig 1.** A Simplified Schematic of the Mercury Cycle in the Environment (3)

It is known that mercury oxidation is the main mechanism of removal of GEM from the atmosphere (5). Thus, in order to better understand Hg cycling in the environment and the impact of point-source atmospheric emissions, it becomes critical to develop instrumentation for determining the chemical speciation of Hg (3). While techniques for GEM sampling and measure-

ment are now quite mature (8), methods for GOM measurements are still under development. Therefore, the development of a highly sensitive detector of GOM for atmospherically relevant concentrations (i.e. low picograms per cubic meter,  $\text{pg}/\text{m}^3$ ) is a high priority research topic (6, 8-10). Three common methods for measuring ambient GOM (8, 10-12) have been developed: i) refluxing mist chambers; ii) ion-exchange membranes behind particulate filters, and iii) potassium chloride (KCl)-coated tubular denuders. The advantages and disadvantages of these methods have also been reported previously (10). The annular denuder method has so far been the most widely employed among these methods being developed because of the high-time resolution achieved and its relative simplicity (8). Recently, the KCl denuder technique has come under fire for the susceptibility to trap GOM to other atmospheric constituents (e.g. ozone) (12). Thus, a denuder-based aircraft instrument with a higher temporal resolution (15 min) measurement of GOM was deployed alongside a new difference technique for aircraft measurements of GEM and GOM (13). This difference technique determines GOM concentrations as total atmospheric mercury (TAM) minus GEM. While TAM was measured by a Tekran 2537 CVAFS that pulled sample air through a pyrolyzer at  $500^\circ\text{C}$ , GEM was measured with another Tekran 2537 CVAFS that pulled sample air through a KCl denuder and a particulate filter. This difference method is a relatively fast technique for measurement of GOM, compared to other methods such as KCl denuder. The results obtained from the difference method have shown a linear consistent correlation with GOM concentrations determined by KCl denuder. Nevertheless, 15% ( $\pm 13\%$ ) discrepancy was found between the two methods, suggesting the difference technique typically measures higher GOM than the KCl denuder method (13). Given the success of the difference technique for measurement of oxidized mercury in the remote troposphere (13), it holds significant promise for measurement of GOM and/or Hg-P in other regions of the atmosphere.

Several studies have shown that urban/industrial areas can be subject to greater deposition of mercury from local anthropogenic Hg sources than regional/global sources (10, 14). Nevertheless, mercury measurements in the urban atmosphere are quite limited compared with those in the remote and rural areas (6). Mercury speciation in the urban atmosphere is even less frequently studied (6), and to our current knowledge, no studies have been based on the difference technique proposed herein. Therefore, the objectives of this research project are: 1) to develop an efficient difference technique based on the aircraft experiment for the accurate measurements of GOM and GOM+Hg-P in the urban areas of Montreal; 2) to study the diurnal, seasonal and temporal variability of urban atmospheric mercury species; 3) to verify the efficiency of this method by comparing with the KCl denuder method; and 4) to identify and quantify the

main mercury species in GOM using the thermal decomposition method by comparison with the known mercury standards such as  $\text{HgCl}_2$  and  $\text{HgBr}_2$ . Mercury speciation information from this study will be used to estimate mercury emissions from Montreal to the troposphere, and will be used to assess the impact of these emissions on the cycling of this element on the local, regional, and global scale.

## METHODS

### GENERAL METHOD FOR THE MEASUREMENTS OF GOM

Simultaneous measurements of RGM and Hg-P (and GEM) were performed by conversion to  $\text{Hg}^0$  for detection using a Tekran 2600 CVAFS automated Hg measurement system (Tekran Inc., Toronto, Ontario, Canada). The principle implies that passing an air stream through a thermal oven heated at  $500^\circ\text{C}$  decomposes GOM and Hg-P to  $\text{Hg}^0$ ; and GEM is measured by bypassing the oven and introducing the air stream directly into the CVAFS. The Tekran 2600 was set to measure  $\text{Hg}^0$  every four minutes using EPA method 1631 (15), which is the method associated with the CVAFS Tekran 2600 software for determination of Hg in the range of 0.5–100 ng/L (15). The EPA 1631 method has been widely used in our laboratory as we have used this method and revised versions during the last decade. The method detection limit (MDL) for Hg is three times the standard deviations of blank measurements, which are presented in the results section.

By determining the difference of hot versus ambient air measurements, we are expected to obtain reliable measurements of the amount of GOM in the urban air, which is described by equations (1) to (3):

$$\text{Hg}_{500\text{C}}^0 = \text{Hg}_{\text{air}}^0 + \text{Hg}_{\text{OxHg}}^0 \quad (1)$$

$$\text{Hg}_{\text{AT}}^0 = \text{Hg}_{\text{air}}^0 \quad (2)$$

$$\text{Hg}_{500\text{C}}^0 - \text{Hg}_{\text{AT}}^0 = \text{Hg}_{\text{OxHg}}^0 \quad (3)$$

where:

$\text{Hg}_{500\text{C}}^0$  is the quantity of elemental mercury measured by passing air through the thermal oven at  $500^\circ\text{C}$  ( $\text{ng}\cdot\text{m}^{-3}$ );

$\text{Hg}_{\text{AT}}^0$  is the quantity of elemental mercury in air at ambient temperature ( $\text{ng}\cdot\text{m}^{-3}$ );

$\text{Hg}_{\text{OxHg}}^0$  is the amount of mercury present in air as oxidized mercury ( $\text{ng}\cdot\text{m}^{-3}$ ).

## INSTRUMENT SETUP

### THERMAL DECOMPOSITION UNIT

The unit for thermal decomposition of oxidized mercury consists of 1/4" (0.635 cm) borosilicate glass inlet surrounded by an Omegaux brand oven that is capable of reaching temperatures up to  $1800^\circ\text{F}$  ( $982^\circ\text{C}$ ). However, for the purpose of this study, we kept the temperature of the oven consistently at  $500^\circ\text{C}$ . The temperature of the glass inlet is continuously measured with a type K thermocouple. A simplified schematic diagram of the instrument setup is illustrated in Fig. 2. The outlet of the decomposition unit is connected to a brass two-way valve that connects directly to the CVAFS. The flowmeter has been set to  $300\text{ mL}\cdot\text{min}^{-1}$  to control the flow of the sample into the instrument by regulating the pump flow. The valve is also connected to a Teflon tube, which draws air directly from the ambient environment. By toggling the two-way valve manually, ambient air may thus be sampled either directly at ambient temperature or at elevated temperature through the decomposition unit.

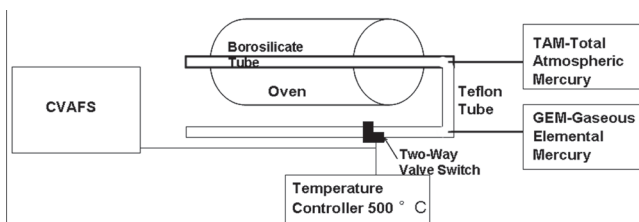


Fig 2. A Simplified Schematic Diagram of the Experimental Setup: Thermal Decomposition Unit and CVAFS

### CVAFS

The Tekran model 2600 CVAFS is a very stable, sensitive ultra-trace mercury analyzer, and has been recognized for its high sensitivity, low noise and stability (18). The technique differs from the more conventional atomic absorption (AA) and mass spectrometric (MS) techniques in that it is more sensitive (levels in the low parts per quadrillion (ppq) range) (19), more selective, inexpensive, and is linear over a wide range of concentrations (15). In addition, CVAFS is used in the measurement of trace amounts of volatile mercury and makes use of the unique characteristic of mercury that allows vapor measurement at ambient temperature.

### CALIBRATION

The Tekran 2600 mercury analyzer was calibrated in the laboratory room using manual  $\text{Hg}_0$  injections. The manual  $\text{Hg}_0$  injections were done by injecting a series of known volumes ( $2\ \mu\text{L}$ ,  $10\ \mu\text{L}$ ,  $25\ \mu\text{L}$ ,  $50\ \mu\text{L}$ ,  $75\ \mu\text{L}$  and  $100\ \mu\text{L}$ ) of mercury-saturated air withdrawn from a reservoir headspace into the Tekran 2600 analyzer injection port. The calibration unit reservoir temperature

was kept at ambient temperature (23 °C). At this temperature, the vapor pressure of mercury is 16.879 pg / $\mu\text{L}$  according to the mercury saturation table (20).

## VERIFICATION OF THE THERMAL DECOMPOSITION EFFICIENCY

To estimate the thermal decomposition efficiency of this developed analytical technique at converting GOM to  $\text{Hg}^0$ , two methods were used. Ontario Hydro Method (OHM) and insertion of a glass wool tube were employed for direct comparisons, which are illustrated in Figs. 3 and 4 respectively.  $\text{HgCl}_2$  and  $\text{HgBr}_2$  diffusion sources were connected to the inlet of the thermal decomposition unit to introduce GOM-rich gas streams into the thermal decomposition unit.

### ONTARIO HYDRO METHOD (OHM)

This method was used to monitor oxidized (and elemental) mercury fluxes from industrial sources (21). A 1 Normal KCl solution was prepared by dissolving 7g KCl crystals into an impinger flask containing 100 mL Milli-Q water. A 20%  $\text{SnCl}_2$  solution was prepared by adding 20 g of  $\text{SnCl}_2 \cdot 2\text{H}_2\text{O}$  and 10 mL concentrated HCl to 100 mL Milli-Q water. The solutions were purged overnight with mercury-free argon to remove all traces of Hg, and then stored by covering with parafilm. Air was drawn by the CVAFS through the  $\text{HgCl}_2$  source and KCl solution for several samplings, followed by injection of 1 mL of  $\text{SnCl}_2$  into the impinger, and analysis of the impinge headspace by CVAFS. After 20 minutes, another 0.5 mL of  $\text{SnCl}_2$  was injected into the impinger, and the headspace was again analyzed for  $\text{Hg}^0$ . Injection of  $\text{SnCl}_2$  and monitoring of  $\text{Hg}^0$  produced was repeated several times for each  $\text{HgCl}_2$  collection.

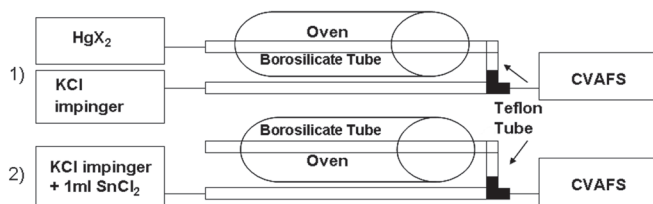


Fig 3. A Simplified Schematic Diagram of the Ontario Hydro Method (OHM) for Efficiency Test

### INSERTION OF A GLASS WOOL TUBE

As the Ontario Hydro method does not provide a quick check of the efficiency of the thermal decomposition unit due to various contaminations, a simpler method was pursued by introducing a glass wool tube into the thermal decomposition instrumental unit. This method works due to the principle that GOM sticks to glass wool while GEM does not. This efficiency method was deployed in two steps. Firstly, a glass wool tube was added between the oven unit and the CVAFS, and a mercury

halide standard ( $\text{HgCl}_2$  or  $\text{HgBr}_2$ ) was connected to the oven to measure the amount of GOM into the thermal decomposition unit along with most of the GOM stuck to the glass wool. Secondly, the glass wool tube was directly inserted inside the thermal decomposition unit and without the mercury halide standard; the amount of GOM stuck to the glass wool from the previous run was measured by running with the CVAFS a second time. The sum of these two-step measurements can be then used to estimate the thermal decomposition efficiency.

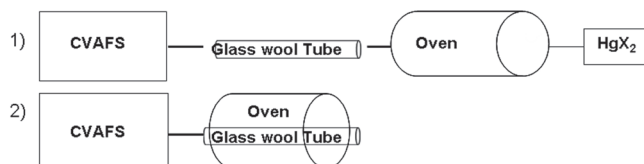


Fig 4. A Simplified Schematic Diagram of the Efficiency Test Using the Method of the Glass Wool Tube Insertion

## ATMOSPHERIC GOM MEASUREMENTS IN DOWNTOWN MONTREAL

The study site was moved from the indoor laboratory to an open area on the 5<sup>th</sup> floor terrace of the science building, Pavillon Président-Kennedy at UQAM. This was done to truly investigate the amount of oxidized mercury in atmosphere as this would better reflect regional anthropogenic activities involving mercury use (22). Ambient air GEM concentrations were also measured overnight in order to get a diurnal cycle of mercury in the urban area.

## RESULTS AND DISCUSSION

### CALIBRATION CURVE

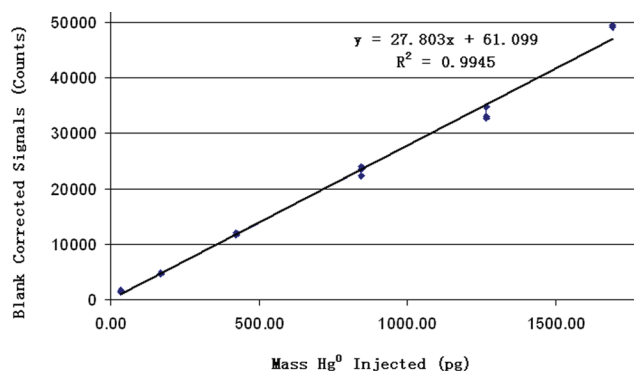


Fig 5. Calibration Curve for the Determination of the Amount of  $\text{Hg}^0$  Injected into CVAFS

The slope from this calibration curve (Fig. 5) was found to be 27.803 counts/pg, from which the amount of  $\text{Hg}^0$  injected can be calculated by following equations (4)-(6):

$$\frac{C}{m} = \text{Hg}^0 \quad (4)$$

$$\frac{t_{\text{sampling}}}{60 \text{ sec/min}} Q = \text{Vol.}_{\text{Hg}^0} \quad (5)$$

$$\frac{\text{Hg}^0}{\text{Vol.}_{\text{Hg}^0}} = \text{Hg}^0 \quad (6)$$

where:

C is the number of peak area counts per run (counts)  
m is the slope of the calibration curve in counts per picogram (counts/pg)

$\text{Hg}^0$  is the amount of Hg in picogram (pg)

$t_{\text{sampling}}$  is the method sampling time in seconds (sec)

Q is the sampling flow rate in liters per minutes (L/min)

$\text{Vol.}_{\text{Hg}^0}$  is the volume of Hg in liters (L)

Deviations of the analyzer between calibrations were less than 15%, which suggested that this calibration was well done according to the EPA 1631 manual (15). The variability of most of the data in this study was around 3% and had an average counts/room air run of 880 counts/run, which corresponds to 31.6 pg  $\text{Hg}^0$  using equation (4). Then, using the 70 second sampling time at 0.3 L/min; this gives a concentration of  $\text{Hg}^0$  in room air of 90.4  $\text{ng}\cdot\text{m}^{-3}$   $\text{Hg}^0$ . This value is larger than the average of GEM measurements found in downtown Montreal over 24 hours, 65.3  $\text{ng}\cdot\text{m}^{-3}$   $\text{Hg}^0$ . However, this value can still be considered within the big range, and shows how the laboratory is filled with a significant amount of mercury versus outside areas. Mercury concentrations posing human health risks are in the range 0.7–4.2 $\times 10^7$   $\text{ng}\cdot\text{m}^{-3}$ ; thus, this shows the mercury levels in our laboratory and in the present atmosphere are still acceptable (16, 17).

## TEMPORAL VARIABILITY OF ATMOSPHERIC GEM IN DOWNTOWN MONTREAL

The reliability of measuring GEM in air limits the capability to detect oxidized mercury as a difference between TAM and GEM. Air measurements had varied stability over short time-periods. This variability can be described with the diurnal cycle (Fig. 6) recorded over 24 hours on July 27 and 28, 2011. The concentrations of elemental Hg (GEM) species tended to be low and stable in the late night time and early morning (between 9:00 PM to 6:00 AM). GEM then started increasing around 6:00 AM until reached its maximum in the afternoon (between

2:00 PM to 5:00 PM), and tended to decrease in the late afternoon and even more from evening time before stabilizing again and reached its minimum at 9 pm. This diurnal pattern indicated that significant temporal variations in concentrations of GEM were observed in the daytime ranging from 21–276  $\text{ng}\cdot\text{m}^{-3}$ , especially in the afternoon. In addition, this diurnal cycle could also reflect highly variable emission patterns from anthropogenic mercury sources during the daytime and the lower emissions at night, when human activity is less. Hence, these results indicate that local anthropogenic sources have significant influence on the levels of the Hg species in the urban atmosphere.

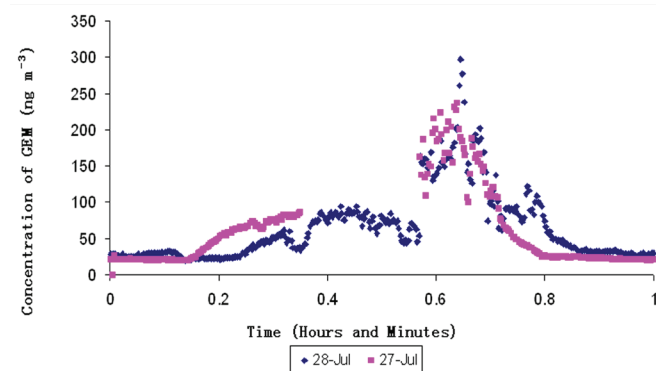


Fig 6. Diurnal Pattern of GEM in Ambient Atmosphere Mercury Species On July 27–28, 2011 for 24 Hours

Moreover, no consistent pattern was observed between fluctuations in TAM hot air measurements and observed variable concentrations of GEM during the afternoon time. This made the determination of GOM difficult during the daytime and could suggest that TAM levels are unrelated to GOM fluctuations, or that variable atmospheric conditions are differentially affecting the various mercury species.

The method detection limit (MDL) for the difference technique according to the results in Fig. 6 is at least 6–50  $\text{ng}\cdot\text{m}^{-3}$ , depending on the variability. This MDL with CVAFS is very high compared to the MDLs found in other related studies using CVAFS, 0.04 and 0.06  $\text{ng}\cdot\text{m}^{-3}$  (6, 13). This suggests that other systematic errors might present that need to be identified and accounted for.

## ATMOSPHERIC GOM MEASUREMENTS IN DOWNTOWN MONTREAL

The average TAM-GEM difference, based on the data collected with significant variations in the afternoons on July 12 and 14, 2011 from noon to 6:30 PM was estimated to be 14.7  $\pm 10.3$   $\text{ng}\cdot\text{m}^{-3}$  (arithmetic mean from eight groups of TAM-GEM differences and 95% confidence intervals). The relatively large error value suggested that further method investigation is required.

## VERIFY THERMAL DECOMPOSITION EFFICIENCY

The Ontario Hydro Method (OHM) was employed at first, and failed to check its efficiency as much higher peak area values were observed when room air was passed through either the KCl or SnCl<sub>2</sub> impinger. This suggests that the solutions themselves might have been contaminated by mercury. As preparation of the new sample standards and solutions is a very time consuming process, we chose to employ a simpler method using a glass wool tube. This new efficiency test was not successfully done at present due to the fact that the incoming flux of GOM was significantly higher than that found in a similar source tested by others (27 pg·min<sup>-1</sup> (8)). However, we believe the latter is a better method since only further decrease of the fluxes from the diffusion sources prior to testing is needed to make this method of efficiency a success.

## CONCLUSION

In conclusion, the difference-thermal decomposition technique has been successfully developed and applied partly to measure GOM in downtown Montreal. Although GOM results were very limited, they have indicated that an urban area is a continuous source of Hg species that potentially impact local and regional TAM levels. Also, local and regional anthropogenic sources contributed significantly to the levels and the distributions of the Hg species in the urban atmosphere (6). Due to the significant fluctuations observed in the afternoon, a clear relationship between atmospheric TAM and GOM has not been established. Thus, the contribution of urban areas to atmospheric Hg budget remains unknown at this point (6), due to lack of experimental data and the large uncertainty on the limited measurements made so far. This suggests more systematic approaches are needed for quantifying the contribution of urban areas to atmospheric Hg.

Future work in the short term could establish an association between TAM and GEM by collecting TAM data overnight, in order to accurately measure the difference GOM results. Moreover, the MDL could be decreased by increasing the flow rate and the method sampling time. In the long term, as the manual switching complicates evaluation of the diurnal variability in GOM over a long period of time and limits the number of measurements, an automated valve could be employed to facilitate the switch and increase the number of measurements. In addition, due to the high incoming flux of GOM, testing the method efficiency using the glass wool tube and investigating the decomposition profiles of different Hg species with varying temperature are difficult at this point. Since the cooling process should in principle decrease the vapor pressure of mercury halides above the source crystals; and therefore, the incoming

flux of GOM, the problem could be resolved by further cooling the sources in a dry-ice ethanol/liquid-nitrogen bath. Furthermore, Hg air sampling should be done not only in downtown Montreal, but also in other areas to investigate and compare the results. Finally, reasons for temporal variations are not apparent. This suggests a need for further investigation and a need to prove the efficiency of the thermal decomposition unit by comparing with the KCl denuder method with ambient air replaced by nitrogen gas during collection, in order to prevent interference by ozone (12).

## ACKNOWLEDGEMENTS

Research consultation with Dr. Daniel Deeds was very much appreciated. I would also like to thank Dr. Parisa Ariya, who reviewed the drafts of this paper and made a considerable number of suggestions for its improvement.

## REFERENCES

1. M. A. Lopez-Anton *et al.* *Fuel* **89**, 629–634 (2010).
2. M. A. Lopez-Anton *et al.* *Fuel Processing Technology* **92**, 707–711 (2011).
3. A. Steffen *et al.*, Polar mercury review paper, *Atmos. Chem. Phys.* **8**, 1445–1482 (2008).
4. The Mercury Cycle, mercury in the environment and water supply, [http://people.uwec.edu/piercech/Hg/mercury\\_water/cycling.htm](http://people.uwec.edu/piercech/Hg/mercury_water/cycling.htm) (Accessed June 17, 2011).
5. W.H. Schroeder, and J. Munthe, *Atmos. Env.* **32**, 5, 809–822 (1998).
6. C-J. Lin *et al.* *Atmos. Env.* **33**, 2067–2079 (1999).
7. X. Song *et al.* *J. Environ. Monit.* **11**, 660–669 (2009).
8. X-B. Feng *et al.* *Anal. Bioanal. Chem.* **376**, 1137–1140 (2003).
9. D.G. Streets *et al.* *Atmos. Env.* **39**, 40, 7789–7806 (2005).
10. M.S. Landis *et al.* *Environ. Sci. Technol.* **36**, 3600–3009 (2002).
11. A.P. Rutter *et al.* *J. Air Waste Manag. Assoc.* **58**, 377–383 (2008).
12. S.N. Lyman, D.A. Jaffe, and M.S. Gustin, *Atmos. Chem. Phys.* **10**, 8197–8204, (2010).
13. P.C. Swartzendruber *et al.* *Environ. Sci. Technol.* **43**, 7484–7489 (2009).
14. B. Liu *et al.* *Atmospheric Environment* **44**, 2013–2023 (2010).
15. W.A. Telliard, Method 1631, Revision C, EPA-821-R-01-024, March 2001.
16. M.G. Cherian, J.G. Hursh, T.W. Clarkson, *Archives of Environmental Health* **33**, 190–214 (1978).
17. C.H. Ngim, S.C. Foo, K.W. Boey, and J. Keyaratnam, *British Journal of Industrial Medicine* **49**, 11, 782–790 (1992).
18. The Tekran Series 2600 Difference, Tekran Instruments Corporation, Toronto, [http://www.tekran.com/files/facts\\_2600\\_r127.pdf](http://www.tekran.com/files/facts_2600_r127.pdf) (Accessed June 17, 2011).
19. Cold Vapour Atomic Fluorescence Spectroscopy, Wikipedia, From Wikipedia, the free encyclopedia, [http://en.wikipedia.org/wiki/Cold\\_vapour\\_atomic\\_fluorescence\\_spectroscopy](http://en.wikipedia.org/wiki/Cold_vapour_atomic_fluorescence_spectroscopy) (Accessed June 17, 2011).

20. Mercury Saturation Table, Tekran Instruments Corporation, Toronto, Canada
21. Sun, J.Q. *et al.* Prepr. Pap.-*Am. Chem. Soc.*, Div. Fuel Chem. **48**, 2, 774 (2003).
22. Hayward, *et al.* Division of Air Quality, Raleigh, NC (2004).

# Protection of the Differentiated Chondrocyte Phenotype during Monolayer Expansion Cultures Using Heat Inactivated Fetal Calf Serum

Tat Fong Ng<sup>\*1</sup>, Mourad Matmati<sup>1</sup>, Thomas M. Quinn<sup>1</sup>

<sup>1</sup>Department of Chemical Engineering, McGill University, 3610 University Street Montreal, Quebec, Canada H3A 2B2

## ABSTRACT

**Introduction:** Autologous Chondrocyte Implantation (ACI) is one successful treatment for osteoarthritic defects (1-4). However, chondrocytes undergo a conversion to a fibroblastic phenotype during their expansion *in vitro*. This process can lead to degradation and failure of the repaired tissue, and is termed “dedifferentiation” (5-9). We hypothesized that culturing chondrocytes in Heat Inactivated Fetal Calf Serum (HIFCS) would lead to a slowing of the process of dedifferentiation. This study specifically examines how HIFCS affects gene expression and proliferation of bovine chondrocytes in short-term monolayer culture. **Methods:** We cultured primary chondrocytes extracted from bovine joints in FCS or HIFCS for four passages (P0-P4). We then analysed the relative gene expression of aggrecan (*agg*), type II-alpha1 collagen (*col2a1*), cartilage oligomeric matrix protein (*comp*), SRY (sex determining region Y)-box 9 (*sox9*), type I-alpha2 collagen (*col1a2*) and Bcl-2-associated X protein (*bax*) using quantitative real-time Polymerase Chain Reaction (qPCR). **Results:** Our results show significant down-regulation of *col1a2* and up-regulations of *agg*, *col2a1*, *comp* and *sox9* in HIFCS cultures when compared to those in FCS cultures. **Discussion:** *Agg*, *col2a1* and *comp* are associated with the synthesis of cartilage matrix molecules while *sox9* is associated with chondrogenesis (5-11). *Col1a2* is associated with the presence of fibrous tissue which lacks the desired mechanical properties (5-9). Therefore, our results suggest that HIFCS can partially protect the chondrocytic phenotype from dedifferentiating to fibroblastic after one passage. To improve upon our results, more experiments are required to reveal the mechanism underlying the protection of chondrocytes offered by the heat inactivation of FCS.

## KEYWORDS

*Autologous Chondrocyte Implantation, articular cartilage, chondrocyte expansion, heat inactivated fetal calf serum*

\*Corresponding author:

tat.ng@mail.mcgill.ca

Received: 2 January, 2012

Revised: 2 March 2012

## INTRODUCTION

Articular cartilage is a dense connective tissue which ensures smooth motion and proper weight transfer in synovial joints. In adult articular cartilage, which is avascular and aneural, nutrients are mainly transported via diffusion instead of direct delivery by blood vessels (12). After an injury, this system can make the *in vivo* natural repair process very difficult to heal itself because of the inefficient delivery of required nutrients and removal of undesired waste by diffusion. Physical or biochemical damage can alter the chondrocytes' phenotype and lead to the formation of

fibrocartilage, which is a mechanically inferior tissue and can be broken down after prolonged use (13).

To recover the native functionality of the injured articular cartilage, one of the tissue engineering techniques is used to assist the healing process – Autologous Chondrocyte Implantation (ACI) (14). It is the most common surgical treatment for cartilage damage since it is economical and technically simple. In ACI, healthy articular chondrocytes are first extracted from patients and then expanded in monolayer cultures, in which all chondrocytes are growing side by side on the same growth surface and none growing on top of another. This *in vitro* chondrocyte proliferation is repeated for multiple passages to reach a minimum density of 15 to 20 million cells before implantation into cartilage defects (1, 3, 15). There are two advantages to this technique. Firstly, the healthy chondrocytes transferred from other patients might be recognized as foreign cells by the immune system of the host patient, which would then trigger immune defense in the recipient. Therefore, the use of autologous cells prevents such negative immune responses and can provide an active repair process to the joint (16). Secondly, only a small quantity of chondrocytes is needed, and they can be extracted from a non-load-bearing site in the patient (17). As a clinical practice, ACI achieves functional recovery for a majority of patients (2–4). However, a critical drawback of this technique is that chondrocytes dedifferentiate during proliferation, which affects the ability of the implanted chondrocytes to regenerate and serve as a long-term functional replacement for the original tissue (5–9).

Since chondrocytes dedifferentiate during their proliferation in monolayer culture, extensive research has revealed relationships between the degree of chondrocytes' dedifferentiation and their corresponding morphology, gene expression profile and proliferation rates. *Col2a1* is the major collagen produced by chondrocytes, and it makes up 50% of all protein in cartilage (18). *Col1a2* is the major collagen produced by fibroblasts, and it is presented in scar tissue, dentin, dermis and tendon (18). When chondrocytes attach to the flat surface of a cell culture dish, their cell structure gradually changes from a spherical to a spindle-shaped morphology after multiple monolayer passages (19, 20). In addition, protein production shifts from *col2a1* to *col1a2* and the proliferation rate increases with higher number of passages (5, 7–9, 10, 21, 22). Although the underlying mechanism of this shift is still poorly understood, previous research has eliminated as a possible cause for the relationship between the cell shape and types of collagen synthesized in passaged monolayer cultures of chondrocytes (23). Researchers believe that the shift in types of collagen initiates in the early stages of *in vitro* expansion (24).

In this project, we hypothesized that chondrocytes expanded in HIFCS would maintain their differentiated phenotype, but would dedifferentiate in FCS. Although morphology, genotype,

cell growth and protein analysis are all essential to understand the underlying mechanism of decelerated chondrocytes dedifferentiation, we focused primarily on genotype and cell growth analysis in this study; morphology and protein analysis were performed by other collaborators in the same laboratory. For genotype analysis, gene expression of *col1a2* indicated the degree of dedifferentiation, and the expression of *agg*, *col2a1*, *comp* and *sox9* reflected the extent of differentiation. *Agg* is a major structural component of articular cartilage that facilitates chondrocyte-chondrocyte and chondrocyte-matrix interactions (25). *Comp* is a noncollagenous ECM protein responsible for collagen fibril formation (26, 27). *Sox9* acts as the first high-mobility-group domain transcription factor that is required for chondrocyte differentiation and cartilage formation (11, 28). *Bax* gene expression was used to see whether a decline in cell proliferation and an increase in cell death were due to the extracellular environment, the heat inactivation of FCS, or intracellular activities (29, 30). Hence, the objectives of this study were to compare the relative gene expression profiles and proliferation rates of articular chondrocytes expanded in monolayer FCS or HIFCS cultures during passaging and determine the minimum number of passages required for the clinical application of ACI.

## EXPERIMENTAL METHODS

### TISSUE HARVEST

Approximately 3–5 g of articular cartilage was first aseptically dissected from each bovine joint provided by a local abattoir. Mixed population of chondrocytes from the superficial and middle zones (top 10–20%) could then be isolated as most of the proliferating chondrocytes were presented in these zones. Chondrocytes were then enzymatically digested from cartilage tissue segments using previously published techniques (31). For each sample, the tissue was minced using a scalpel and digested for 24 h in 20 mL of Dulbecco's Modified Eagle Medium (DMEM) High Glucose 1X (Invitrogen, Grand Island, NY), supplemented with 2 mg/mL type II collagenase (Sigma Aldrich, St. Louis, MO), in an incubator with 5% CO<sub>2</sub> at 37°C. The resulting cell suspensions were strained from undigested tissue debris and cell clumps using a 70 µm pore size polyethersulfone mesh, and the cell density was obtained using a Zeiss Axiovert 40°C microscope with a hemacytometer. Chondrocytes obtained at this stage were considered as a control for comparison with passaged chondrocytes.

### CELL CULTURE

For each donor, a low density of  $1 \times 10^5$  chondrocytes were plated in a 100mm×20mm non-pyrogenic sterile polystyrene cell culture dish (Corning Incorporated, Corning, NY) filled with 6mL of FCS or 6mL of HIFCS. The FCS was composed of DMEM

enriched with 10% Fetal Bovine Serum (FBS) and 1% Prostate Specific Antigen (PSA). HIFCS was prepared with the same protocol, except that the FBS used was first heat inactivated at 56°C for 30mins before mixing with DMEM and PSA (32). In addition to the original 6mL of FCS or HIFCS added in the first day of initial seeding, an extra of 3mL FCS or HIFCS were added after 5 days of initial seeding to provide fresh nutrients. After 10 days, near confluence (~50,000cell/cm<sup>2</sup>) was achieved (33) and cells in both cultures (P0) were isolated by trypsinization using previously published techniques (34). Their cell densities were then obtained by counting the total number of cells in the plastic plate and dividing it by the total volume of FCS or HIFCS added. Then, 1×10<sup>5</sup> P0 chondrocytes were passaged using the same protocol and to the same level of confluency—but for only 5 days due to accelerated proliferation—to obtain P1 chondrocytes. This procedure was repeated a total of four times to obtain P1 to P4 chondrocytes.

### RNA EXTRACTION

Samples of ribonucleic acid (RNA) were extracted from control and P0 to P4 chondrocytes expanded in FCS and HIFCS cultures using Invitrogen RNA isolation protocol as recommended by the manufacturer. The RNA samples were then diluted with diethylpyrocarbonate (DEPC)-treated water (Invitrogen, Carlsbad, CA) and stored at -80°C. Diluted RNA solutions were measured at optical density (OD) 260 for total RNA and at OD 280 for total protein readings using the Eppendorf BioPhotometer Plus. The measured concentrations of diluted RNA solutions can be accepted with minimal accuracy as long as they had RNA-to-protein ratios of 1.8 to 2.2, indicating adequate relative purities (35).

### cDNA SYNTHESIS

RNA was reversed transcribed into complementary deoxyribonucleic acid (cDNA) using qScript™ cDNA Synthesis Kit (Quanta BioSciences, Gaithersburg, MD) as recommended by the manufacturer. In this procedure, 15 μL RNA and nuclease-free water, 1 μL reverse transcriptase and 4 μL Reaction Mix (5x) were mixed together, reversed transcribed at 42°C for 1h, and stored at -20°C. The synthesized cDNA was amplified using PCR and this process can be verified by obtaining proper fragment size in gel electrophoresis. Glyceraldehyde-3-phosphate dehydrogenase (*gapdh*) was used as an endogenous control (31, 36, 38).

### QUANTIFICATION OF GENE EXPRESSION

qPCR is a technique used to simultaneously amplify and quantify the amount of selected DNA sequence presented in a sample. It was performed on a 96-well/plate ABI Prism 7900HT Sequence Detection machine (Applied Biosystems, Foster City, CA) using Standard Cycle SYBR Green qPCR protocol (Quanta Biosciences, Gaithersburg, MD). The total volume (20 μL) of

each PCR reaction consisted of 10 μL PerfeCTa™ SYBR™ Green FastMix™ ROX, 7 μL de-mineralized water (ddH<sub>2</sub>O), 2 μL cDNA, 0.5 μL for each of 20% forward and reverse primers. Table 1 lists the forward and reverse sequences for each primer used (Invitrogen, Carlsbad, CA). Primer sequences for all genes were designed using bovine messenger RNA (mRNA) data published on the National Center for Biotechnology Information (NCBI) website. The qPCR reaction was carried out at 95°C for 10 min (activation), 40 cycles of 95°C for 15 s, 60°C for 20 s and 72°C for 20s (amplification), and 72°C for 1 min (final extension) (37).

### RELATIVE GENE EXPRESSION

Gene expression for *agg*, *col2a1*, *comp*, *sox9*, *col1a2* and *bax* were normalized using the endogenous control gene, *gapdh*, so that the variations in the number of cells per sample became insignificant. The 2<sup>-T</sup> method of relative quantification of gene expression was chosen because it relates the PCR signal of the target transcript in a treatment group to that in an untreated control (38). To obtain the value of *T* from raw *T* data, we used this equation:  $T = (CT, Target - CT, gapdh) Time x - (CT, Target - CT, gapdh) Time 0$ , where our targets were the genes *agg*, *col2a1*, *comp*, *sox9*, *col1a2* and *bax*. To fully comprehend why the amount of target can be calculated by finding 2<sup>-T</sup>, please refer to derivation and explanation written by Livak and Schmittgen (38). Relative gene expression values greater than 1 indicated that the gene of interest was expressed to a greater level than the endogenous gene. Since the expression value of *gapdh* was assumed to be constant among all the chondrocytes analyzed, the relative expression of the gene of interest could be quantified independently of the amount of RNA extracted from chondrocytes in each sample (30, 38).

**Table 1.** Primer sequences used for qPCR analysis

Primers	Forward Sequence (5' to 3') Reverse Sequence (5' to 3')
<i>gapdh</i>	ACCCTCAAGATTGTCAGCAA ACGATGCCAAAGTGGTCA
<i>agg</i>	GCTACCCTGACCTTCATC AAGCTTTCTGGGATGTCCAC
<i>col2a1</i>	AACGGTGGCTTCCACTTC GCAGGAAGGTCATCTGGA
<i>comp</i>	TTCGGAACGCACTGTGG TGCAGGACAGCGGTA
<i>sox9</i>	ACGCCGAGCTCAGCAAGA CACGAACCGCTTCT
<i>col1a2</i>	CATTAGGGGTCACAATGGTC TGGAGTTCCATTTTCACCAG
<i>bax</i>	AACATGGAGCTGCAGAGGAT CAGTTGAGTTGCCGTCAGA

## STATISTICAL ANALYSIS

A total of 6 groups of experiments were performed, each with a sample size of  $n=3$ . Among the 6 groups of experiments, 3 groups were obtained only from chondrocytes without passaging (P0) to determine the baseline effect of HIFCS. The other 3 groups of experiments analyzed all of the passaged chondrocytes (P0 to P4). As a result, a total sample size of  $n=18$  were analyzed for P0 chondrocytes but  $n=8$  were analyzed for P1 to P4 chondrocytes due to a loss of one sample during the first passage. The means and standard error of the mean were calculated using Excel spreadsheet software. Finally,  $z$ -test, F-test and t-test were applied to test the significance of the results. P-values less than 0.05 were deemed to be significant.

## RESULTS

### EFFECT OF HEAT INACTIVATION

In order to test the hypothesis that the heat inactivation of FCS would decelerate chondrocyte dedifferentiation, three analyses were required. The first analysis compared the gene expression of P0 chondrocytes cultured in HIFCS relative to those cultured in FCS. As seen in Fig. 1, the expression of genes *agg*, *col2a1*, *comp* and *sox9* were significantly augmented in HIFCS cultures when compared to that in FCS cultures, while the expression of gene *col1a2* was significantly reduced in HIFCS cultures when compared to that in FCS cultures. In order to assess the effect of heat inactivation of FCS, P0 chondrocytes cultured in HIFCS or FCS was compared to freshly isolated chondrocytes. As shown in Fig. 2, the gene expression of *agg*, *col2a1*, *comp* and *sox9* in HIFCS cultures were significantly decreased when compared to that in FCS cultures; and the expression of gene *col1a2* is significantly increased in HIFCS cultures when compared to that in FCS cultures (all  $P=0.00$ ). *Agg* gene expression in HIFCS was about 54% higher than that in FCS cultures ( $P=0.012$ ) while *col1a2* gene expression in HIFCS cultures was about 42% less than that in FCS cultures ( $P=0.045$ ). As the total yield of P0 chondrocytes was much lower than the minimal requirement for clinical applications, which is about 15 to 20 million cells, multiple passages were essential. The third analysis compared the gene expression of passaged chondrocytes cultured in HIFCS to those cultured in FCS. From Fig. 3, all the gene expression of *agg*, *col2a1*, *comp* and *sox9* were significantly amplified for P0 to P4 chondrocytes in HIFCS cultures when compared to that in FCS cultures, except the *agg* gene expression in P3 chondrocytes. However, when the gene expression of *col1a2* was examined for passaged chondrocytes, only P0 to P1 chondrocytes were significantly declined in HIFCS cultures when compared to that in FCS cultures. Finally, the expression of the *bax* gene was consistently insignificant.

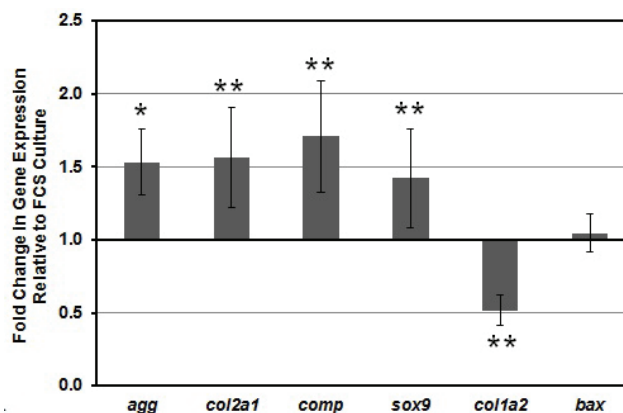


Fig. 1. Gene expression of P0 chondrocytes in HIFCS cultures relative to that of FCS cultures. Values represent mean  $\pm$  standard error of the mean for  $n=18$ . Statistically significant differences are indicated by  $*=P<0.05$  and  $**=P<0.01$ .

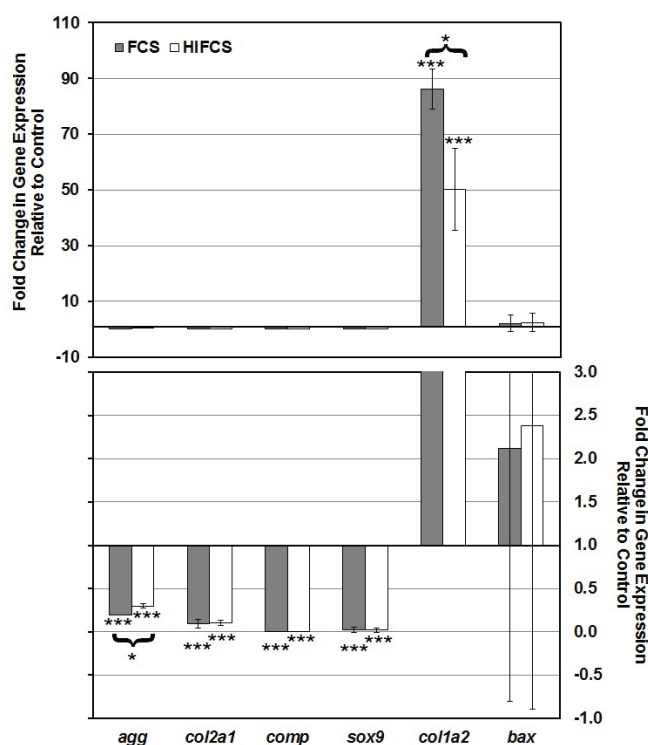


Fig. 2. Gene expression of P0 chondrocytes in FCS and HIFCS cultures relative to that of freshly isolated chondrocytes. Values represent mean  $\pm$  standard error of the mean for  $n=9$ . Statistically significant difference is indicated by  $*=P<0.05$  and  $***=P<0.001$ .

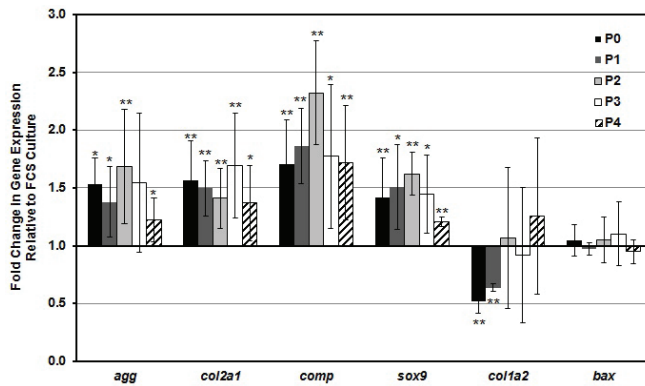


Fig. 3. Gene expression of P0 to P4 chondrocytes in HIFCS cultures relative to that of FCS cultures. Values represent mean  $\pm$  standard error of the mean for  $n=18$  for P0 chondrocytes and  $n=8$  for P1 to P4 chondrocytes. Statistically significant differences are indicated by  $*=P<0.05$  and  $**=P<0.01$ .

### CELL GROWTH PROFILE

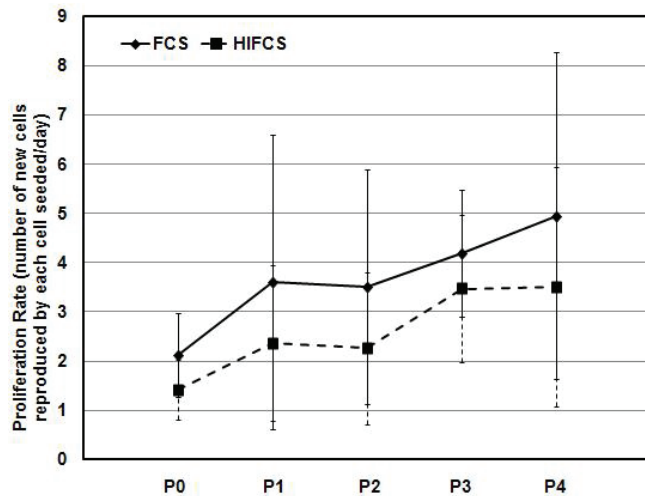


Fig. 4. Proliferation rates (number of new cells reproduced by each cell seeded per day) of P0 to P4 chondrocytes. Values represent mean  $\pm$  standard error of the mean for  $n=9$  for P0 to P2 chondrocytes and  $n=8$  for P3 and P4 chondrocytes.

After investigating the effect of HIFCS on the genotypes of passaged chondrocytes, the proliferation rate and cumulative cell numbers of chondrocytes expanded in all passages were analyzed to give a cell growth profile. Proliferation rate, which was defined as the number of new cells reproduced by each cell seeded initially per unit of time, was plotted in Fig. 4 for all passaged chondrocytes expanded in FCS and HIFCS cultures. Noticeably, chondrocyte proliferation rate increased with the number of passages in both FCS and HIFCS cultures. Additionally, the proliferation rates of FCS cultures were generally higher than the rate in HIFCS

cultures for each passage. Finally, Fig.5 depicts the cumulative cell numbers of P0 to P4 chondrocytes cultured in FCS and HIFCS. It can be observed that the cumulative cell numbers in FCS cultures are always higher than that in HIFCS cultures and this difference is increasing as we passaged the chondrocytes from P0 to P4.

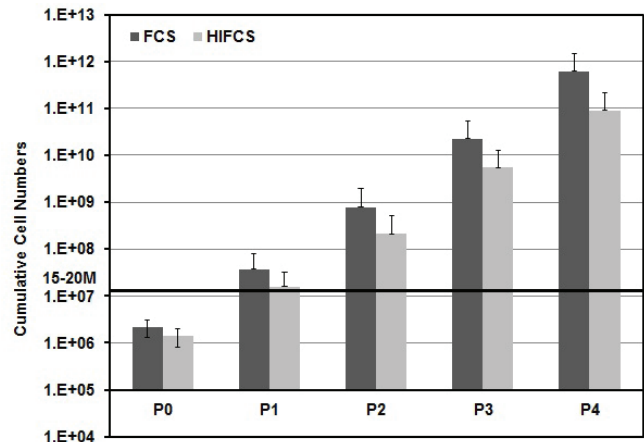


Fig. 5. Cumulative Cell Numbers of P0 to P4 chondrocytes. Values represent mean  $\pm$  standard error of the mean for  $n=9$  for P0 to P2 chondrocytes and  $n=8$  for P3 and P4 chondrocytes. The horizontal line at 15-20M indicates the minimum number of cells required for clinical treatments of cartilage defects.

## DISCUSSIONS

### EFFECT OF HEAT INACTIVATION

Fig. 1 reveals the effect of heat inactivation of FCS on chondrocytes by comparing the gene expression of P0 chondrocytes cultured in HIFCS relative to those grown in FCS. The significant up-regulation of chondrocytic genes (*agg*, *col2a1*, *comp*, *sox9*) and significant down-regulation of fibroblastic gene (*col1a2*) in HIFCS cultures when compared to FCS cultures prove that HIFCS was indeed more effective than FCS in protecting the chondrocytes from dedifferentiation. In addition, the insignificant difference between *bax* gene expression levels in FCS and HIFCS cultures might indicate that the heat inactivation of FCS did not cause fatal damage in cultured chondrocytes' organelles, but the confirmation of this statement required repeated experimentation.

The comparison of gene expression of P0 chondrocytes cultured in FCS or HIFCS relative to that of freshly isolated chondrocytes was necessary to determine the degree of dedifferentiation in *in vitro* chondrocyte cultures and provide an indirect assessment of the effect of heat inactivation of FCS. From Fig.2, the significant down-regulation of all chondrocytic genes (*agg*, *col2a1*, *comp* and *sox9*) and strong up-regulation of fibroblastic gene (*col1a2*) shows that the dedifferentiation of chondrocytes was initiated

in the beginning of *in vitro* expansion in both FCS or HIFCS cultures. Again, the relative insignificance of *bax* gene expression might imply that the cell death that occurred in both FCS and HIFCS was mainly caused by the extracellular environment instead of intracellular activities, but more experiments would be needed in order to prove this statement.

The comparison between gene expression of passaged chondrocytes cultured in HIFCS and those grown in FCS cultures demonstrated how multiple passages impacted the effectiveness of HIFCS. In Fig. 3, the consistency of significantly up-regulated chondrocytic genes (*agg*, *col2a1*, *comp* and *sox9*) for P0 to P4 chondrocytes in HIFCS cultures when compared to that in FCS cultures implied that the advantageous protection offered by HIFCS was persistent for four passages. This protection by HIFCS was unaffected by passaging as no increasing nor decreasing trend could be observed in these chondrocytic gene expression. Nevertheless, when the fibroblastic gene expression (*col1a2*) was examined for passaged chondrocytes, the down-regulation of the gene *col1a2* was significant for only one passage. This infers that P2 to P4 chondrocytes are not practical for clinical treatments as the implantation of them will not be functional in patients' joints. Finally, the expression of the *bax* gene was consistently insignificant which might provide additional suggestion that HIFCS did not kill the intracellular organelles of cultured chondrocytes. However, more experiments are needed to reduce the error rate and acquire accurate results in order to draw affirmative conclusion about the effect of passaging on the efficiency of HIFCS for chondrocytes.

## CELL GROWTH PROFILE

After investigating the effect of HIFCS on the genotypes of passaged chondrocytes, the proliferation rate and cumulative cell numbers of chondrocytes expanded in all passages were analyzed to give a cell growth profile. Proliferation rate was plotted in Fig. 4 for all passaged chondrocytes expanded in FCS and HIFCS cultures. Noticeably, chondrocyte proliferation rate increased with the number of passages in both FCS and HIFCS cultures. Additionally, the proliferation rates of FCS cultures were generally higher than the rate in HIFCS cultures for each passage. In spite of the fact that higher proliferation rates in FCS cultures were achieved when compared with that in HIFCS cultures in Fig. 4, this difference is statistically insignificant, which might suggest that the slower dedifferentiation rate observed in HIFCS chondrocyte cultures was not due to lower proliferation rates. This result might be crucial because decelerated dedifferentiation of chondrocytes originating from a lower proliferation rate is scientifically reasonable; any findings that could not rule this out should not be accepted as a new discovery. Lastly, Fig. 5 shows that the chondrocytes needed to be expanded in HIFCS cultures for at least one passage to reach the clinically required minimum of 15 to 20 million cells for ACI therapy.

## CONCLUSIONS

This project aims to investigate the effect of heat inactivation of Fetal Calf Serum (FCS) on the process of chondrocytes' dedifferentiation. Bovine articular chondrocytes were isolated and expanded through monolayer cell culture supplemented with either FCS or Heat Inactivated Fetal Calf Serum (HIFCS) for four passages. The study indicates that the addition of HIFCS to the culture media limits the dedifferentiation from chondrocytes to fibroblasts for one passage. Furthermore, we show that one passage creates sufficient amounts of chondrocytes for clinical applications. Nevertheless, our results, while potentially significant, are preliminary. More experiments will be required to determine whether the limited dedifferentiation in HIFCS cultures is originated from lower proliferation of chondrocytes. Moreover, further experiments are necessary to disclose the mechanism underlying the protection of chondrocytes by the heat inactivation of FCS in order to advance successful clinical applications of articular cartilage regeneration.

## ACKNOWLEDGEMENTS

The author would like to thank Dr. Mourad Matmati and Prof. Thomas Quinn for proposing this interesting project. This research was supported by the Canada Research Chairs and NSERC-CIHR Collaborative Health Research Projects programs.

## REFERENCES

1. M. Brittberg *et al.* *N. Engl. J. Med.* **331**, 889-895 (1994).
2. M. Brittberg *et al.* *Clin. Orthop.* **391** (Suppl), S337-348 (2001).
3. S. Marlovits *et al.* *Knee. Surg. Sports Traumatol Arthrosc* **13**, 451-457 (2004).
4. M. Ronga, F.A. Grassi, P. Bulgheroni, *Arthroscopy Cell* **20**, 79-84 (2004).
5. R. Mayne, M.S. Vail, P.M. Mayne, E.J. Miller, *J. Biol.* **73**, 1674-1678 (1976).
6. P.D. Benya, S.R. Padilla, M.E. Nimni, *J. Biochem.* **16**, 865-872 (1977).
7. P.D. Benya, S.R. Padilla, M.E. Nimni, *Cell* **15**, 1313-1321 (1978).
8. P.D. Benya, J.D. Shaffer, *Cell* **30**, 215-224 (1982).
9. D.G. Stokes *et al.* *J. Biochem.* **360**, 461-470 (2001).
10. F. Zaucke, R. Dinsler, P. Maurer, M. Paulsson, *J. Biochem.* **358**, 17-24 (2001).
11. W. Bi, J.M. Deng, Z. Zhang, R.R. Behringer, B. de Crombrughe, *Nat. Genet.* **22**, 85-89 (1999).
12. J. Ryu, B.V. Treadwell, H.J. Mankin, *Arthritis. Rheum.* **27**, 49-57 (1984).
13. E.B. Hunziker, *Osteoarthr. Cartil.* **7**, 15-28 (1999).
14. E.M. Darling, K.A. Athanasiou, *Annal. Biomed. Eng.* **31**, 1-11 (2003).
15. P. Cherubino, F.A. Grassi, P. Bulgheroni, M. Ronga, *J. Orthop. Surg.* **11**, 10-15 (2003).

16. M. Brittberg *et al.* *J. Bone Joint Surg* **85**, 109-115 (2003).
17. E.B. Hunziker, *Osteoarthr. Cartil.* **10**, 432-463 (2001).
18. E.J. Miller, *Mol. Cell. Biochem.* **13**, 165-192 (1976).
19. H.G. Coon, *Proc. Natn. Acad. Sci. U.S.A.* **55**, 66-73 (1966).
20. S. Chacko, J. Abbot, S. Holtzer, H. Holtzer, *J. Exp. Med.* **130**, 417-442 (1969).
21. M.H. Zheng *et al.* *Int. J. Mol. Med.* **13**, 623-628 (2004).
22. J. Glowacki, E. Trepman, J. Folkman, *Proc. Soc. Exp. Biol. Med.* **172**, 93-98 (1983).
23. K. von der Mark, V. Gaus, H. von der Mark, P. Muller, *Nature* **267**, 531-532 (1977).
24. E.M. Darling, K.A. Athanasiou, *J. Orthop Res.* **23**, 1128-1138 (2005).
25. C. Kiani, L. Chen, Y.J. Wu, A.J. Yee, B.B. Yang, *Cell Res.* **12**, 19-32 (2002).
26. T. Saxne, D. Heinegard, *Br. J. Rheumatol.* **31**, 583-591 (1992).
27. M. Wislowska, B. Jablonska, *Clin. Rheumatol.* **24**, 278-284 (2005).
28. E. Wright *et al.* *Nature Genet.* **9**, 15-20 (1995).
29. P. Mocetti *et al.* *Tissue & Cell* **33**, 1-7 (2001).
30. S.J. Wang *et al.* *J. Rheumatol.* **33**, 615-619 (2006).
31. E.M. Darling, J.C.Y. Hu, K.A. Athanasiou, *J. Orthop. Res.* **22**, 1182-1187 (2004).
32. R.H. Zubler, G. Lange, P.H. Lambert, P.A. Miescher, *J. Immunol.* **116**, 232-235 (1976).
33. E.M. Darling, K.A. Athanasiou, *J. Orthop. Res.* **23**, 425-432 (2005).
34. I.R. Freshney, *Culture of Animal Cells* (Wiley, New York, ed. 3, 1994), p.p. 310-348.
35. K.R. Brodtkin, A.J. Garcia, M.E. Levenston, *Biomater.* **25**, 5929-5938 (2004).
36. B. Bau *et al.* *Arthritis. Rheum.* **46**, 2648-2657 (2002).
37. L. Zhen *et al.* *J. Orthop. Res.* **26**, 1230-1237 (2008).
38. K.J. Livak, T.D. Schmittgen, *Methods* **25**, 402-408 (2001).

# Genomics of Regulatory Elements: A special focus on the HoxA Gene Cluster and Experimental Techniques.

Akal Sethi\*<sup>1</sup>

<sup>1</sup>Department of Biochemistry, McGill University

## ABSTRACT

**Introduction:** The regulation of gene expression plays a pivotal role in maintaining proper biological functions as well as creating cell diversity. Many regulatory elements are cis-acting and act over thousands of base pairs to affect the expression of their target gene. The development of novel techniques has provided a wealth of information into spatial chromatin organization, with the potential to unravel the mechanism of relatively uncharacterized regulatory elements, such as repressors and insulators. **Discussion:** This review will highlight examples of genomic regulation, such as Beta-globin loci and the HoxA cluster, as well as discuss advantages and disadvantages of the currently employed experimental techniques. Moreover, genomic regulation as it pertains to human disease will also be discussed.

---

\*Corresponding author:

sethi.akal@gmail.com

Received: 2 January 2012

Revised: 2 March 2012

## INTRODUCTION

Almost every component of molecular and organismal biology encompasses some sort of regulation of gene expression, often in temporal and tissue-specific manners. The organization of complex biological systems requires substantial regulatory information and capabilities. Embryonic development in any species requires the coordinated expression of a multitude of genes and their corresponding gene products to create and structure subtle gradients that lead to proper apportioning of limbs, nerves, and organs. It was postulated over 40 years ago that the level of genomic regulation was proportional to the complexity of the organism (1). However, the current tools to search for elements involved in regulation are still primitive in nature and a method to easily identify genomic regulatory elements in a regular and reliable fashion has yet to be established (1,2). Some regulatory elements such as promoters can be easily identified by their dutiful position at the 5' end of genes and thus thousands have been determined by standard techniques such as chromatin immunoprecipitation and cDNA sequencing (3). Although promoters are relatively simple to study, other regulatory elements such as enhancers, repressors, insulators and barriers are more difficult to elucidate due to their lack of defined positions.

Although the theory of *cis* (intrachromosomal) regulation was favored before the human genome was sequenced, the ideas of a *trans* (interchromosomal) approach or a combination of the two were also put forward. Analyses of multiple loci under long range control yielded significant insight into how exactly genes were regulated in *cis*. One of the most characterized loci is the globin locus that lies upstream of the beta-globin gene. According to van Assendelft et al., this locus regulates beta-globin in a manner independent of the chromosomal integration site (4). Understanding of locus control regions led to a greater understanding of enhancers via a combined approach of transgenic mouse assays and bacterial artificial chromosome-mediated transgenics. In the transgenic mouse assays, regions of interest were fused with a LacZ reporter gene, which allows for visualization of gene expression in temporal and spatial arrays confirming predetermined expression patterns. Deletion analysis identified enhancers spanning hundreds of base pairs within thousands of base pairs (5,6). Bacterial artificial chromosomes (BAC's), originally developed to help sequence the human genome, can be used in transgenic assays to span kilobases of genomic DNA. In such instances, several BAC's can be paired together in a quantitative fashion allowing for a representation of the genomic DNA and thus provide an ideal control for experiments on genomic DNA (7). Such studies culminated in the discovery of enhancers of the Bmp5 gene. These enhancers operate at large distances from the promoter (>200kbp) and were among the first distal acting regulatory elements to be discovered (7). It is vital to develop a greater understanding of long-range regulation as the amount of evidence for position-effect diseases is staggering (8).

These studies, conducted before full sequencing of the human genome, indicated many intrachromosomal regulatory activities that were further corroborated by more modern comparative techniques. Combinations of other vertebrate genome studies and high-throughput screens have identified novel distal regulatory sequences and are slowly coloring in the dark areas of genomic structure. This review will discuss the different classes of regulatory elements that have thus far been clearly characterized as well as the novel techniques that are providing new insights into the foundations and architecture of genomic regulation. Additionally, how regulation leads to human disease will be a point of focus. More specifically, the role of Hox gene regulation in potential malformations and disease will be discussed in greater detail, and this will serve as a primary example throughout the review.

## TYPES OF DISTAL REGULATORY ELEMENTS

There have been several types of regulatory elements identified. The word "identified" is apt since techniques have proven their

existence, rather than elucidated their function. Although the promoter is not a distal regulatory element in the majority of instances, its vital role in gene expression warrants its mention. As Noonan and McCallion phrase it, "the promoter is the fulcrum around which transcription pivots," in other words, the promoter is the site where basal transcriptional units such as polymerases and the overall holoenzyme form (2). The promoters determine the direction and orientation of transcription as described by Maston et al. (9). The long-range regulatory elements discussed in this review have been typified by their responses to certain biological assays and thus can be interpreted as broad categories rather than specifically determined elements.

Elements that positively regulate transcription are known as enhancers. Enhancers are position independent as they may be distal or proximal to the promoter of the target gene. Although the exact manner in which enhancers up-regulate transcription is still unknown, one sensible model proposes that enhancers attract transcription factors that together promote the assembly of transcription machinery at the promoter of the target gene. In this proposed model, the chromatin loops together bringing the enhancer and the promoter into proximal contact despite being base pairs away in the linear genome (10). A prime example of enhancer capability is the enhancer of the Sonic Hedgehog (Shh) gene, a Hox gene. Shh is one of the genes responsible for creating the posterior-anterior axis in developing limbs in vertebrate embryos. Deletion analysis in the enhancer, approximately 1 MB from the Shh promoter in an intron of the LMBR1 gene, caused errors in Shh expression in the anterior of the limb and led to disease and malformation in the form of preaxial polydactyly (11,12). Complete deletion of the enhancer resulted in a loss in expression and degeneration of limbs (13). The data obtained from the Shh enhancer shows the importance of enhancers in development.

Elements that negatively regulate transcription are known as negatively-acting elements. To date, most of the regulatory elements identified are enhancers because they are easy to find with clear and straightforward biological assays. These assays include the transgenic insertion of reporter genes that can be analyzed by luciferase assays, fluorescent microscopy for GFP tagged products, or bright field microscopy of beta-galactosidase stained tissues. One of the more intriguing facts about regulatory elements such as enhancers and negatively-acting elements is their variability when exposed to different environmental stimuli. Stress, diet, hormones, temperature and lack of nutrients can all vary regulatory elements' actions through cellular signals (14). This point is important to consider as it indicates that the results seen from assays measuring regular element activity have an impact on the function performed by that element. Under these circumstances, the binding of certain

transcription factors can cause various enhancers to be bound by repressor proteins and thus function as negatively-acting elements (2,15,16).

Insulators, or barriers, are positioned such that the adjacent genes do not interfere with each other's expression. There are two mechanisms by which insulators can separate regulation: barrier activity or enhancer blocking (EB) activity, both of which are measured by synthetically designed assays (17). Barrier activity is the ability of a sequence to create definitive borders between regions of euchromatin and heterochromatin, while EB activity limits the positive regulatory ability of enhancers by acting in a position-dependent manner. The first vertebrate insulator to be thoroughly studied and understood was the HS4 sequence in the chicken beta-globin locus that shows both barrier and EB activity in assays involving reporter genes. In this case, a protein that binds insulator sequences, the CCCTC-binding factor (CTCF), aids in EB activity (18,19). It is worth mentioning that CTCF also mediates expression within the same gene locus. In the mouse beta-globin locus, CTCF binding along with the joining of certain regulatory elements yields an active chromatin hub ACH. Deletion of CTCF or its binding sites led to instability of the ACH (20). The study of mouse and chicken globin loci, in combination with other vertebrate globin loci has led to a general consensus that the binding of CTCF is nearly mandatory for enhancer blocking activity in vertebrates. On the other hand, vertebrate barrier activity still seems to be relatively independent of CTCF binding suggesting that vertebrate barrier and EB activity act through independent mechanisms. However, it is still clear that insulators can be comprised of enhancer blockers, barriers, or both.

## HOX A CLUSTER

Although CTCF contact is vital to proper expression and transcription for beta-globin loci, not all genes follow this trend, as some require the disintegration of contacts for activity. The *HoxA* locus is a prime example of such an instance. It is heavily regulated and is thus a cluster of great interest due to its constantly changing genomic architecture and function (21). *HoxA* is part of the *Hox* gene family, one that is highly conserved and encodes for transcription factors responsible in the regulation of development (22). Although there are 4 *Hox* clusters accounting for a total of 39 genes located on separate chromosomes, the *HoxA* cluster is one of the most characterized and pertinent and is located on chromosome 7. It codes for a total of 11 transcription factors. *Hox* genes obtained a claim to fame upon the discovery of how, during development, the spatial orientation of the genes on the chromosomes mimic the gene expression itself in the developing limb. In other words,

*Hox* genes found at the 5' end of the cluster would be expressed in the posterior and much later in development than genes located at the 3' end (23,24). The spatial and temporal expression results suggest that chromatin structure as well as regulatory elements play key roles in controlling *Hox* gene clusters (25,26). Additionally, it has been found that silencing *Hox* genes is essential, as overexpression can lead to disease (see below). Specifically, during active transcription of *HoxA* genes, looping of chromatin is absent compared to its palpable existence during transcriptional silencing (9). The *HoxA* locus provides an example of the variability of regulation when compared to the beta-globin loci in vertebrate tissues.

## DETERMINATION OF CHROMATIN ORGANIZATION

Although this review focuses more on modern day techniques, it would be remiss not to mention the technique that provided much of the information regarding spatial chromatin organization. DNA fluorescence in situ hybridization (DNA-FISH) uses complementarity to hybridize a DNA probe to DNA that has been chemically fixed to a glass slide. The DNA probe contains an antigen for a fluorescent antibody, which may be visualized by epifluorescent microscopy. Using a multitude of DNA targets and different fluorescent antibodies, it is possible to determine the position of genomic locations. Although DNA-FISH has low resolution compared to more modern and advanced techniques, it is a highly accepted method in measuring *in vivo* contacts within single cells. Chromosome conformation capture (3C) has become one of the basic and most functional methods in ascertaining the organization of chromatin as well as helping to understand the connection between gene expression and organization (27,28). Traditionally, 3C can be organized into five steps. The first step consists of chemically fixing cells with formaldehyde or some other crosslinking reagent to capture chromatin in its current structure and thus provide a picture of chromosomal architecture. The second step involves digestion with restriction enzymes. The use of enzymes releases pieces of DNA that were close together due to the cross linking agent. The third step consists of a ligation of the fragments favoring the ligation of ones that were cross-linked close together. The fourth step eliminates all bound proteins and contaminants resulting in a library in which products are comprised of fragments that were close together in nuclear space. The frequency of these products is inversely proportional to the ligated fragments distance in linear organization. The final step of 3C quantifies the individual ligated fragments by PCR and gel electrophoresis, or quantitative PCR and melting curve analysis (29,30). Although 3C yields high-resolution results, it is relatively low throughput and covers small genomic domains. However, some of these disadvantages have been remedied in offshoot techniques of 3C.

Chromosome conformation capture carbon copy (5C) is a derivative of the 3C technique, but provides a more high throughput method (31-34). A normal 3C library is generated; however, the difference lies in the way the analysis is conducted after generation of the library. In contrast to 3C, in which analysis is done by PCR gel detection, in 5C, the 3C libraries are transformed into 5C libraries and then studied by microarrays. The transformation from 3C to 5C libraries is mediated by annealing and subsequent ligation of primers that match 3C ligation points thus allowing for quantitative detection of 3C products. These “carbon copies” are amplified by PCR and then analyzed by microarrays. 5C cannot identify contacts without knowledge of the region of interest, as it requires the predicted 3C junctions in order to create a 5C library. However, this method still has significant value due to its high-throughput capability.

Hi-C is a technique created to ascertain all long-range DNA contacts at the same time (35). After fixation and digestion as usual in such techniques, Hi-C deviates by filling in the overhangs created by the restriction enzymes, and labels some of the inserted nucleotide with epitopes. Normal ligation is then performed followed by sonification to minimize fragment size. The Hi-C products with epitopes are quarantined by affinity chromatography and then analyzed on high-throughput methods, allowing the mapping of all cis and trans chromosomal contacts.

## LONG RANGE REGULATION IN DISEASE

Genomic rearrangements or mutations in regulatory sequences have been found to play roles in human disease (8). Many cis regulatory sequences have been clinically identified by examining the DNA of patients with certain disease phenotypes. By analyzing these abnormalities at the chromosome organizational level, new insights were proposed regarding wild-type chromosomal architecture (8). Mutations that disrupt promoter regulation usually lead to some form of misexpression and thus, most likely a disease (8). There are certain ways in which mutations can lead to disease. For example, genetic evidence may suggest an associated with a certain disease phenotype. Similarly, structural mutations (deletions, insertions, translocations, rearrangements) may be close to a gene vital in the prevention of human disease. Furthermore, the disease phenotype could result from variation within the potential disease and such variation can account for some of the disease risk (8,9). An example of a disease phenotype resulting from an anomaly in long range regulation is the deletion of an enhancer sequence approximately 900 kb upstream of the POU3F4 promoter, which leads to X-linked deafness (36,37). Campomelic dysplasia can be attributed to a mutation in an enhancer of

SOX9 and as stated above, preaxial polydactyly results from a deletion in the Shh enhancer (12,38).

It has been found that diseases associated with the Hox cluster arise from a combination of errors in epigenetic mechanisms and errant long-range regulation (39). In the case of HSC, HoxA9 is up-regulated by increased enhancer activity and decreased methylation, which in turn affects the activity of many Hox genes that play a role in acute myeloid leukemia.

## CONCLUSION

Although gene regulation is commonly thought of and measured in transcriptional output, the actual transcriptional control is mediated via chromosomal structure and regulatory elements. Significant advancements have been made in the study of regulatory elements such as enhancer sequences, while repressors and insulators are not as well characterized. Hopefully, models of gene regulation such as beta-globin loci and the HoxA cluster, in combination with novel techniques such as 5C and Hi-C, will help construct a blueprint of spatial chromatin organization and identify new regulatory elements. Advances in these regards would assist in the battle against diseases involving developmental malformations and cancer by providing an understanding into the disease mechanism, thus providing a foundation for the development of a cure.

## ACKNOWLEDGEMENTS

A special thank you to Dr. Josee Dostie for giving me the opportunity to be in her lab, Dr. Soizik Berlivet for patiently teaching me all the techniques and the theory behind them, and to Jennifer Crutchley, David Wang and James Fraser for answering my incessant questions.

## REFERENCES

1. Britten RJ, Davidson EH, *Science*, **165**, 349-5, (1969).
2. Noonan, J. P. and A. S. McCallion, *Annu. Rev. Genomics Hum. Genet.*, **11**, 1-23, (2010).
3. Cooper SJ, Trinklein ND, Anton ED, Nguyen L, Myers RM, *Genome Res.*, **16**, 1-10, (2006).
4. Blom van Assendelft G, Hanscombe O, Grosveld F, Greaves DR, *Cell*, **56**, 969-77, (1989).
5. Frasch M, Chen X, Lufkin T, *Development*, **121**, 957-74, (1995).
6. Malicki J, Cianetti LC, Peschle C, McGinnis W, *Nature*, **358**, 345-47, (1992).
7. DiLeone RJ, Marcus GA, Johnson MD, Kingsley DM, *Proc. Natl. Acad. Sci. USA*, **97**, 1612-17, (2000).

8. Kleinjan DA, Lettice LA, *Adv. Genet.*, **61**, 339–88, (2008).
9. Maston GA, Evans SK, Green MR, *Annu. Rev. Genomics Hum. Genet.*, **7**, 29–59 (2006).
10. Dekker J, Rippe K, Dekker M, Kleckner N, *Science*, **295**, 1306–11, (2002).
11. Lettice LA, Heaney SJH, Purdie LA, Li L, de Beer P, *et al*, *Hum. Mol. Genet.*, **12**, 1725–35, (2003).
12. Lettice LA, Horikoshi T, Heaney SJH, van Baren MJ, van der Linde HC, *et al*, *Proc. Natl. Acad. Sci. USA*, **99**, 7548–53, (2002).
13. Sagai T, Masuya H, Tamura M, Shimizu K, Yada Y, *et al*, *Mamm. Genome*, **15**, 23–34, (2004).
14. McGrane MM, *J. Nutr. Biochem.*, **18**, 497–508, (2007).
15. Murayama A, Kim M-S, Yanagisawa J, Takeyama K-I, Kato S, *EMBO J*, **23**, 1598–608, (2004).
16. Perissi V, Aggarwal A, Glass CK, Rose DW, Rosenfeld MG, *Cell*, **116**, 511–26, (2004).
17. Gaszner M, Felsenfeld G, *Nat. Rev. Genet.*, **7**, 703–13, (2006).
18. Crutchley, J. L., X. Q. D. Wang, *et al*, *Biomarkers in Medicine*, **4**, 611–629, (2010).
19. Chung JH, Whiteley M, Felsenfeld G, *Cell*, **74**, 505–1, (1993).
20. Splinter E, Heath H, Kooren J *et al*, *Genes Dev.*, **20**, 2349–2354, (2006).
21. Fraser J, Rousseau M, Shenker S *et al*, *Genome Biol.*, **10**, R37, (2009).
22. Krumlauf R. *Cell*, **78**, 191–201, (1994).
23. Kmita M, Duboule D, *Science*, **301**, 331–333, (2003).
24. Duboule D, Morata G, *Trends Genet.*, **10**, 358–364, (1994).
25. Morey C, DA Silva NR, Perry P, Bickmore WA, *Developmental*, **34**, 909–919, (2007).
26. Chambeyron S, Bickmore WA, *Genes Dev.*, **18**, 1119–1130, (2004).
27. Miele A, Dekker J, *Methods Mol. Biol.*, **464**, 105–121, (2009).
28. Miele A, Gheldof N, Tabuchi TM, Dostie J, Dekker J, *Current Protocols in Molecular Biology*. (Wiley, Hoboken, 2006).
29. Hagege H, Klous P, Braem C *et al*, *Nat. Protoc.*, **2**, 1722–1733, (2007).
30. Abou El Hassan M, Bremner R, *Nucleic Acids Res*, **37**, E35, (2009).
31. Dostie J, Richmond TA, Arnaout RA *et al*, *Genome Res*, **16**, 1299–1309, (2006).
32. Dostie J, Zhan Y, Dekker J, *Current Protocols in Molecular Biology* (Wiley, Hoboken, 2006)
33. Dostie J, Dekker J, *Nat. Protoc.*, **2**, 988–1002, (2007).
34. Van Berkum NL, Dekker J, *Methods Mol. Biol.*, **567**, 189–213, (2009).
35. Lieberman-Aiden E, Van Berkum NL, Williams L *et al*, *Science*, **326**, 289–293, (2009).
36. de Kok YJ, Merkx GF, van der Maarel SM, Huber I, Malcolm S, *et al*, *Hum. Mol. Genet.*, **4**, 2145–50, (1995).
37. de Kok YJ, Vossenaar ER, Cremers CW, Dahl N, Laporte J, *et al*, *Hum. Mol. Genet.*, **5**, 1229–35, (1996).
38. Pfeifer D, Kist R, Dewar K, Devon K, Lander ES, *et al*, *Am. J. Hum. Genet.*, **65**, 111–24, (1999).
39. Barber, B. A., M. Rastegar, *Annals of Anatomy - Anatomischer Anzeiger* **192**, 261–274, (2010).
40. J. Borrow, A.M. *et al*, *Nat. Genet.*, **12**, 159–167, (1996).
41. B. Argiropoulos, R.K. Humphries, *Oncogene*, **26**, 6766–6776, (2007).

# The role of anticyclones in replenishing surface cold air and modulating freezing rain duration

Sophie Splawinski<sup>\*1</sup>, John R. Gyakum<sup>1</sup>, Dr. Eyad H. Atallah<sup>1</sup>

<sup>1</sup>Department of Atmospheric and Oceanic Sciences, McGill University, Montreal, Quebec, Canada

## ABSTRACT

**Introduction:** Freezing rain (FZRA), a hazardous meteorological phenomenon, is associated with airflows from both cyclones and anticyclones. Though researchers have placed primary emphasis on the cyclone's role in FZRA, we intend to examine the anticyclone's role in transporting near-surface cold air. More specifically, we study its impact on the duration of FZRA in a region of orographically enhanced vulnerability, namely at Quebec City (YQB), located in the St-Lawrence River Valley (SLRV). This region is an active zone of freezing rain due to orographic influences that promote pressure-driven channeling. **Methods:** Within the SLRV region, we define a severe event using a minimum duration threshold of six hours and found 47 severe freezing rain cases during a 30-year period (1979-2008). We then partitioned these cases into categories based on precipitation phase change and 850hPa geostrophic relative vorticity. **Results:** We found that the duration of freezing rain is determined in large part by the intensity and location of the anticyclone. **Discussion:** The anticyclone enhances pressure-driven channeling, and this channeling provides the replenishment of cold air at the surface required to maintain FZRA. Identifying these anticyclonic features provides a novel approach to determine the potential duration of FZRA events.

### Keywords

Severe weather: Any weather phenomena related to the disruption of social services, property damage, and/or loss of life. Freezing rain: A meteorological phenomenon characterized supercooled water freezing on contact due to a shallow layer of sub-zero temperatures at the surface and a warm layer aloft. Anticyclone: A large scale, clockwise-rotating (northern hemisphere) weather system characterized by generally calm weather and high pressure at its center. St-Lawrence River Valley: A low-lying topographical region encompassing the Montreal and Quebec City areas, extending into southern Ontario and eastward to the Gaspé Peninsula. Pressure-driven Channeling: Valley winds that are driven by the pressure gradient aligned along the axis of the St-Lawrence River Valley.

## KEYWORDS

*Severe weather, freezing rain, anticyclone, St-Lawrence River Valley*

\*Corresponding author:

sophie.splawinski@mail.mcgill.ca

Received: 2 January, 2012

Revised: 2 March 2012

## INTRODUCTION

### MOTIVATION

Freezing rain (FZRA) is a meteorological phenomenon that poses many hazards to the general population and resources, including damage to crops and city infrastructure (1). It occurs when the vertical structure of the atmosphere has a shallow layer of sub-zero temperatures at the surface and a warm layer of above zero temperatures aloft. The warm layer must be thick enough to entirely melt snowflakes falling from the clouds, which then freeze upon contact with the surface. The occurrence of FZRA in

SLRV is significant because the SLRV is one of the most climatologically active areas for FZRA in North America (3). Severe FZRA events have inflicted billions of dollars in damage to the province of Quebec (4). It is therefore of significant importance that research be conducted to better understand their occurrence.

## OBJECTIVES

FZRA forecasts given by Environment Canada utilize models issued by the Canadian Meteorological Centre. Splawinski *et al.* (2) introduce the importance of the SLRV in pressure-driven channeling and identify the general synoptic structure of severe FZRA events in YQB. This paper attempts to further identify the influence of specific features, namely the low-level jet and anticyclone, on the duration of severe FZRA events. Knowledge of these features' impact on duration may enable better forecasting techniques, thereby significantly improving watches and warnings issued to the public for FZRA events.

## PREVIOUS WORK

While most past research on FZRA in eastern Canada has focused mainly on climatology and case studies of specific events, only Ressler *et al.* (2012), Splawinski *et al.* (2011), and Rauber *et al.* (1994, 2001) focus on the frequency of synoptic scale weather patterns associated with freezing participation. And though Splawinski *et al.* (2011) provide an overview of conditions necessary for FZRA formation, the vertical structure and significance of individual features associated with FZRA were not examined. Following the work of Splawinski *et al.* (2011), this research focuses solely on the small structures of freezing rain, as opposed to freezing drizzle, whose synoptic-scale structures are distinctively different from those of freezing rain (1, 4, 5, 6).

## RESULTS

### APPROACH AND DATA

The data set and initial parameters of this study are the same as those used in Splawinski *et al.* (2011) (2). A 30-year period (1979-2008) was chosen and analyzed using hourly surface observations at Jean-Lesage International Airport in Quebec City, QC. Events with a minimum duration of six hours were categorized as severe events; of the 218 individual cases, 47 were determined to be severe.

Analyses were conducted using the North American Regional Reanalysis (NARR) dataset (6), and the associated graphics were then created using the General Meteorological Package (GEMPAK) version 5.7.2 (8). Finally, WRPlot View (9) was used in conjunction with Environment Canada surface data to create wind roses, which plot the distribution of magnitude and direction of winds at a location for a specific time.

## METHODS AND PARTITIONING TECHNIQUE

Specific precipitation phase changes are associated with distinct vertical structures of the atmosphere; therefore, the 47 individual severe events were partitioned into six categories (Table 1) based on the observed phase change over a three-hour period at the end of FZRA.

Phase Change	P (SLRV)	PN (SLRV)	UP (NS)	UP (EW)	Total
Rain (RA)	2	7	9	0	18
Snow (SN)	5	0	1	0	6
FZDZ (freezing drizzle)	1	1	5	2	9
CLD+ve (no precipitation with an increase in temperature at phase change)	1	3	3	0	7
CLD-ve (no precipitation with a decrease in temperature at phase change)	2	1	1	0	4
CLDst (no precipitation with no change in temperature at phase change)	0	1	0	2	3

**Table 1.** Partitioning of the 47 severe events, based on categories (Phase change) and sub-categories (850hPa flow).

Flow	Description
P(SLRV)	Perturbed flow, within the St-Lawrence River Valley
PN(SLRV)	Perturbed flow, north of the St-Lawrence River Valley
UP (NS)	Unperturbed, meridionally-oriented (South-North) flow
UP (EW)	Unperturbed, zonally-oriented (West-East) flow

**Table 2.** Definitions of the four flows obtained using geostrophic relative vorticity. Table 1 initially categorizes events based on phase change, then on the 850hPa geostrophic relative vorticity.

These events were then further partitioned into four sub-categories, based on 850 hPa cyclonic geostrophic relative vorticity (Table 2). This quantity is proportional to the horizontal Laplacian of the geopotential height field, as shown by equation (1),

$$\xi_g = \frac{1}{f_0} \nabla_p^2 \Phi \quad (1)$$

Where  $\xi_g$  is the geostrophic relative vorticity,  $f_0$  the Coriolis parameter, and  $\Phi$  the geopotential height field. In simpler terms,  $\xi_g$  refers to the local spin of air parcels, and  $\Phi$  describes elevation-adjusted force of gravity. These four distinct flows (Fig. 1a-1d) were observed using a minimum threshold of  $24 \times 10^{-5} \text{s}^{-1}$ . Perturbed flow, characterized by vorticity maxima and maximum curvature at 850hPa, is observed in two distinct patterns. Perturbed flow within the valley (P (SLRV)) is categorized by vorticity maxima and maximum curvature centered along the axis of the SLRV. (Fig. 1a). There is also a distinct perturbed flow and associated vorticity and curvature maxima (PN (SLRV)) centered to the North of the SLRV around the James Bay region (Fig. 1b). Surface pressure patterns were used to distinguish the two flows; the P(SLRV) category having a SW-NE oriented

axis relative to the SLRV in contrast with the NW-SE axis of orientation of the PN(SLRV) category. Unperturbed flow, characterized by a lack of organized vorticity maxima and associated with a straight-line 850hPa flow, was also observed in two categories. The meridional flow (UP(NS)) has a southerly wind flow and an east-west anticyclone-cyclone couplet (Fig. 1c), whereas the zonal flow is characterized by an easterly flow with a north-south couplet.

For the purposes of this paper, specific cases were chosen from each of the four subcategories mentioned above. To be able to provide a representative choice, wind roses of actual wind speed ( $\text{ms}^{-1}$ ) and direction, as well as the 1000-850hPa critical thickness lines (1300m) were created for all events in each subcategory. The 1000-850 hPa critical thickness line of 1300m is a winter

precipitation index based on a climatological-mean value. The coherence among individual cases allows for one case to be chosen at random, while remaining representative of each sub-category.

Sub-categories display weakening wind speeds at the time of phase change (Fig. 2b, f), and/or a distinct wind shift (Fig. 2d,h). This is significant because it relates back to the pressure-driven channeling (12, 13) responsible for the required shallow layer of cold air at the surface.

## METEOGRAMS (THICKNESS AND TEMPERATURE PLOTS)

We examined specific changes in temperature, winds, and thicknesses over YQB, prior to analyzing surface and upper level graphics. The thickness of a column of air relates to the virtual

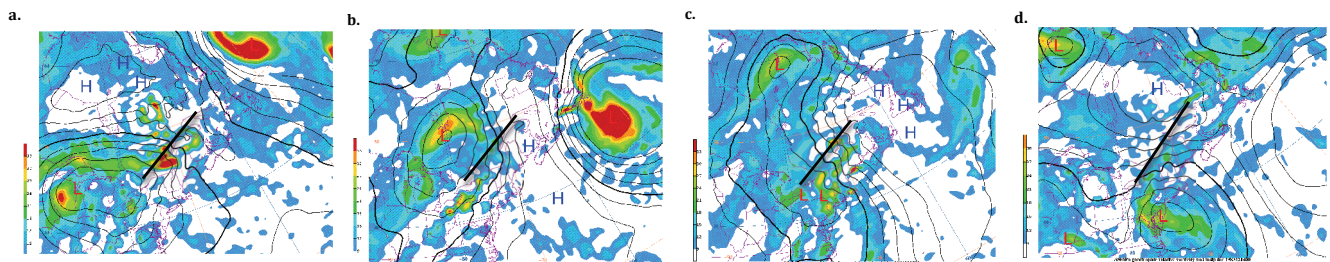


**Figure 1.** 850hPa Geostrophic Relative Vorticity ( $10^{-5}\text{s}^{-1}$ ) and Sea-Level Pressure (SLP, solid black contour of 4 hPa). The black arrow defines the axis of the SLRV. The minimum threshold of  $24 \times 10^{-5}\text{s}^{-1}$  is shaded in lime green. **1a.** P (SLRV): Maxima of cyclonic vorticity located within the SLRV. **1b.** PN (SLRV): Maxima of cyclonic vorticity located N of the SLRV. **1c.** UP (NS): Straight-line north-south oriented geostrophic flow with small, disorganized vorticity maxima. **1d.** UP (EW): Straight-line east-west oriented geostrophic flow with a north-south couplet of high and low pressure.

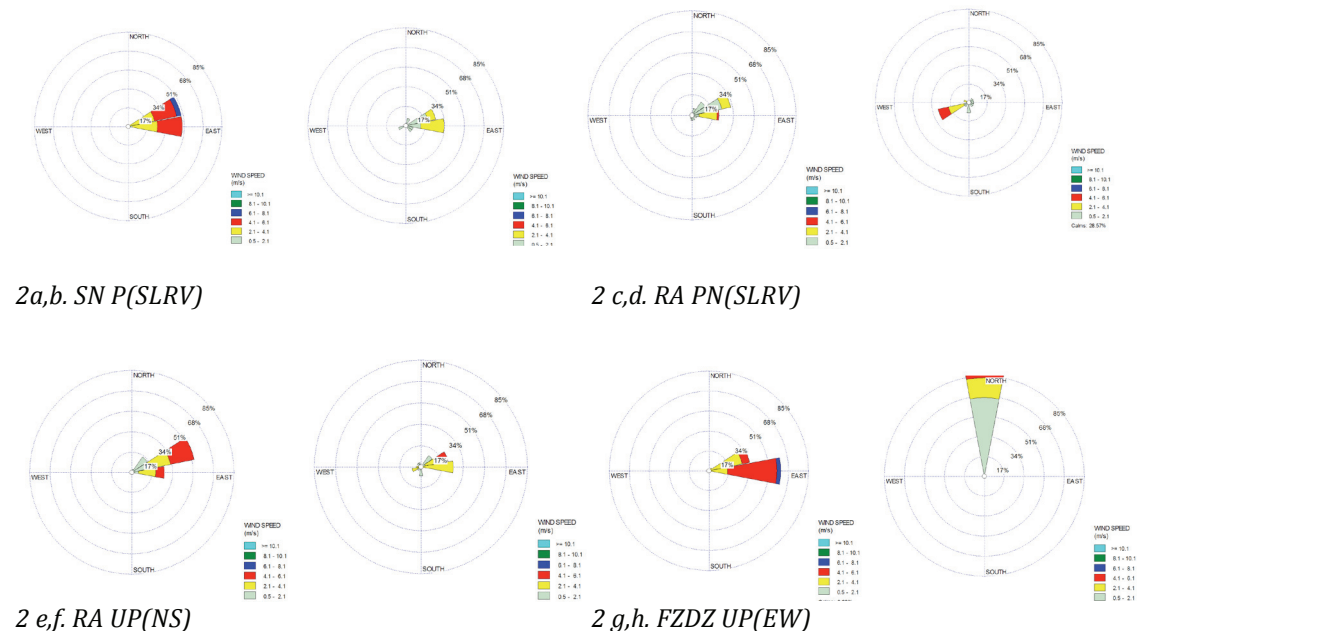


**Figure 2.** Wind roses of surface winds at YQB comprised of all events within that subcategory for at the time of onset and phase change of FZRA, respectively. The rose points in the direction from which the wind is blowing, the concentric circles showing the percentage of time associated with each direction, smaller circles indicating small percentages. The various shades of the rose depict associated wind speeds ( $\text{ms}^{-1}$ ) with darker shades showing successively stronger winds.

temperature (adjustment applied to actual temperature to take into account reduction in air density due to the presence of water vapor<sup>1</sup>) of that column through the hypsometric equation (2),

$$\ln\left(\frac{p_1}{p_2}\right) \frac{R(T_v)}{g} = z_2 - z_1 \quad (2)$$

where  $z_2 - z_1$  is the thickness of the column,  $g$  is gravity,  $R$  is the gas constant for dry air, and  $p_1$  and  $p_2$  are the pressures of the given layers. As the mean virtual temperature of the column increases, the thickness of the column bounded by  $p_1$  and  $p_2$  increases, and vice versa.

Fig. 3a. SN P(SLRV) case (1997.01.05/12Z-1991.01.06/12Z)

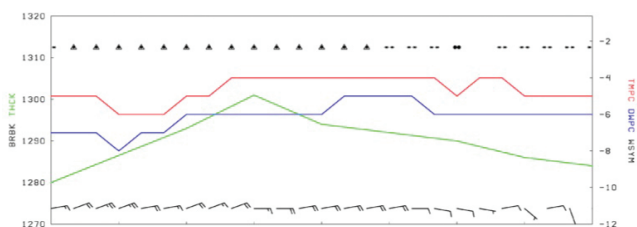


Fig. 3b. RA P(NSLRV) case (1988.03.09/12Z-1988.03.10/12Z)

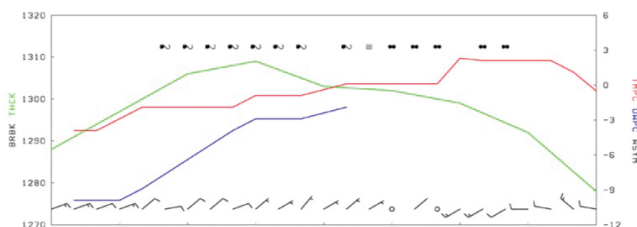


Fig. 3c. RA UP(NS) case (1989.12.31/00Z-1999.01.01/00Z)

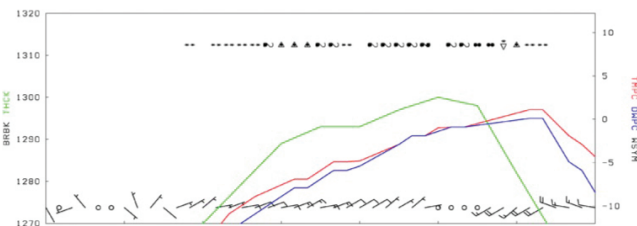
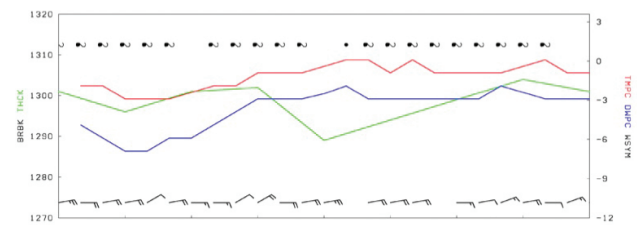


Fig. 3d. FZDZ UP(EW) case (1983.12.14-00Z-1983.12.15/00Z)



Figures 3a-d. Meteogram analyses: 1000-850hPa thickness (green line, m, with scale on left), surface temperature (red line, deg C, scale on right), dewpoint temperature (blue line, deg C, scale on right), wind barbs of standard meteorological convention, weather symbols at the top of the plot. Vertical lines coincide with figures shown below.

Figure 3a, showing the meteogram for the SN P(SLRV), indicates that 1000-850hPa thickness remains between 1280-1300m. Temperatures and winds do not vary substantively throughout the entire period. The thickness declines at the end of FZRA, coinciding with a phase change to snow. Figure 3b depicts the meteogram for the RA PN(SLRV). At the time of phase change into rain, winds predominantly from the NE throughout the event become calm and show a distinct shift to the SW after the changeover occurs. Temperatures then increase from 0 to 3 deg C as the rain continues. However, thicknesses continuously decrease at phase change.

The RA UP(NS) case (Fig. 3c) shows temperature variations of as much as 10 deg C throughout the duration of the event. Thickness trends are positive throughout the event, and only decrease once phase change occurs. At phase change, there is a distinct wind shift once again from the NE to the SW, indicating the loss of pressure-driven channeling.

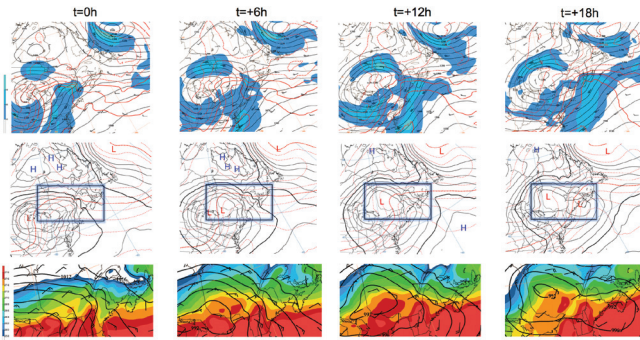
Finally, in the FZDZ UP(EW) event (Fig. 3d), we see consistency among all variables. Especially noteworthy is the maintenance of northeasterly winds throughout the entire event, allowing for temperatures to remain below zero with the maintenance of cold air replenishment at the surface. The 1000-850 hPa thickness also remains almost constant (between 1290-1305m).

### CASE STUDY MAP ANALYSES

To assess the influence of the anticyclone on the duration of freezing rain, we focus primarily on the atmosphere's height difference (or thickness) between the 850 and 1000 levels, more typically 1500m AGL. The shallow layer of cold air at the surface is often decoupled from the warm layer at 850hPa aloft, with each layer having unique thermodynamic structures.

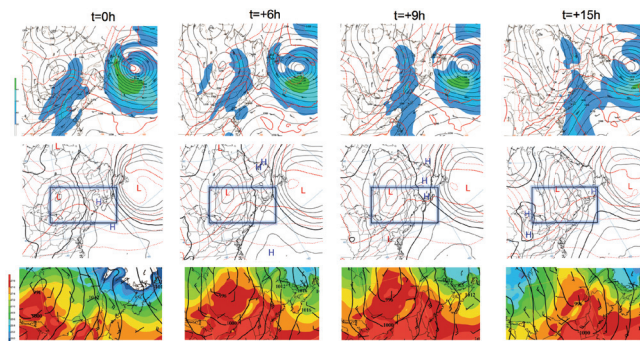
Each of the four case studies chosen is partitioned into four time intervals, starting with the onset and ending at the time of phase change. This allows for the analysis of the synoptic scale flow progression, and for the importance of the SLRV and the anticyclone in the maintenance of FZRA to be highlighted.

Figure 4a identifies a P(SLRV) event with a changeover to snow. At the onset of FZRA (4a.1), the 850hPa flow depicts the presence of a low-level jet (LLJ), with its attendant warm air advection and tropical moisture transport. At the surface, YQB is situated within the warm sector of the cyclone, and is flanked to the north by an anticyclone whose clockwise rotation provides the replenishment of cold air required to maintain FZRA. As the cyclone progresses to the NE, the ridge gradually weakens over northern Quebec as it retreats over northern Hudson Bay. At phase change (Fig. 4a.4), the passage of a cold front and its associated large thickness falls provide a changeover from FZRA to SN. The anticyclone, meanwhile, has weakened and is no longer in a position to provide wind channeling.



**Figure 4a:** Time evolution of the SN P(SLRV) event. The onset of the event is depicted by  $t = 0$  h, and the phase change occurs in the 4<sup>th</sup> panel. Top row: shaded regions indicate 850hPa wind speeds greater than 30knots ( $15\text{ms}^{-1}$ ), 1000-850hPa thickness (solid black contour interval of 30m), 850 hPa isotherms (contour interval of 4 deg C, with red solid indicating values greater than or equal to 0 deg C, red dashed indicating temperatures colder than 0 deg C), with plotted winds in the standard meteorological convention. Middle row: Sea-level pressures (solid black contour interval of 4 hPa, with bold contour showing the 1008 hPa isobar), and 1000-500hPa thickness (dashed contour interval of 60m, with the bold contour indicating the 5400m value). The blue box identifies the region shown in the bottom row. Bottom row: Surface potential temperature (shaded, in K), sea-level pressure (solid contour interval of 4 hPa), and plotted surface winds of standard meteorological convention.

Figure 4b identifies a P(NSLRV) event with a changeover to rain. In this case (Fig. 4b.1), the 850 hPa low center is located farther north and temperatures at YQB at the same level are still above the melting point. At the surface, the anticyclone is structured meridionally and as the low tracks eastward, the anticyclone gradually weakens. At phase change (Fig. 4b.4), there is a loss of pressure-driven channeling along the SLRV due to the weakening of the anticyclone and the passage of the center of the low over YQB. This translates into a wind shift seen in the wind roses (Fig. 2d), from NE to SW. The loss of channeling, combined with the latent heat of fusion from the surface, and the lack of a cold front passage, triggers the changeover from FZRA to rain (RA).



**Figure 4b:** Time evolution of the SN P(SLRV) event. The onset of the event is depicted by  $t = 0$  h, and the phase change occurs in the 4<sup>th</sup> panel. Top row: shaded regions indicate 850hPa wind speeds greater than

30knots ( $15\text{ms}^{-1}$ ), 1000-850hPa thickness (solid black contour interval of 30m), 850 hPa isotherms (contour interval of 4 deg C, with red solid indicating values greater than or equal to 0 deg C, red dashed indicating temperatures colder than 0 deg C), with plotted winds in the standard meteorological convention. Middle row: Sea-level pressures (solid black contour interval of 4 hPa, with bold contour showing the 1008 hPa isobar), and 1000-500hPa thickness (dashed contour interval of 60m, with the bold contour indicating the 5400m value). The blue box identifies the region shown in the bottom row. Bottom row: Surface potential temperature (shaded, in K), sea-level pressure (solid contour interval of 4 hPa), and plotted surface winds of standard meteorological convention.

An UP(NS) event with a changeover into rain is shown in Fig. 4c. Unperturbed categories are associated with strong LLJs that penetrate deep into northern QC. However, the strong anticyclone is anchored just offshore of the Maritime provinces, which manages to offset the warm air advection aloft and latent heat of fusion at the surface, once again with pressure-driven channeling. Sea-level pressure fields indicate that the low deepens without moving eastward, maturing into a well-developed cyclone by phase change (Fig. 4c.4). This intensification also leads to an increase in LLJ speeds throughout the period. Furthermore, the anticyclone gradually travels farther into the Atlantic, where it can no longer sustain the pressure gradient required to maintain cold air replenishment at the surface. The loss of cold air advection at the surface combined with YQB remaining in the warm sector of the cyclone at phase change allows for a change of phase into rain.

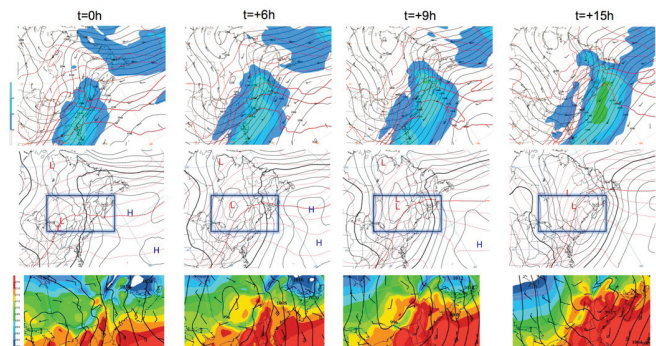


**Figure 4c:** Time evolution of the SN P(SLRV) event. The onset of the event is depicted by  $t = 0$  h, and the phase change occurs in the 4<sup>th</sup> panel. Top row: shaded regions indicate 850hPa wind speeds greater than 30knots ( $15\text{ms}^{-1}$ ), 1000-850hPa thickness (solid black contour interval of 30m), 850 hPa isotherms (contour interval of 4 deg C, with red solid indicating values greater than or equal to 0 deg C, red dashed indicating temperatures colder than 0 deg C), with plotted winds in the standard meteorological convention. Middle row: Sea-level pressures (solid black contour interval of 4 hPa, with bold contour showing the 1008 hPa isobar), and 1000-500hPa thickness (dashed contour interval of 60m, with the bold contour indicating the 5400m value). The blue box identifies the region shown in the bottom row. Bottom row: Surface potential temperature (shaded, in K), sea-level pressure (solid contour interval of 4 hPa), and plotted surface winds of standard meteorological convention.

Figure 4d identifies an UP(EW) event with a changeover to freezing drizzle (FZDZ). The synoptic pattern at the onset of FZRA (Fig. 4a.1) shows a well-developed cyclone along the eastern coast of the United States, coupled with an anticyclone over northern Quebec. The duration of the event is 24h, which stems from both the anticyclone and cyclone's relatively static position, creating a blocking pattern. This pattern allows for continuous replenishment of cold air in the SLRV at the surface from the anticyclone, and warm air advection at 850hPa from the cyclone. As the event progresses, the anticyclone slowly tracks off the coast of Labrador, while the cyclone continues its northerly track. At phase change (Fig. 4d.4), the anticyclone is no longer in a position to maintain the pressure-driven channeling at the surface, cutting off the source of cold air. YQB remains south of the 5400m critical thickness threshold used to differentiate between rain and snow, and a change of phase into FZDZ occurs. Evidently, during the process of weakened channeling, the atmospheric structure becomes more conducive to facilitating FZDZ.

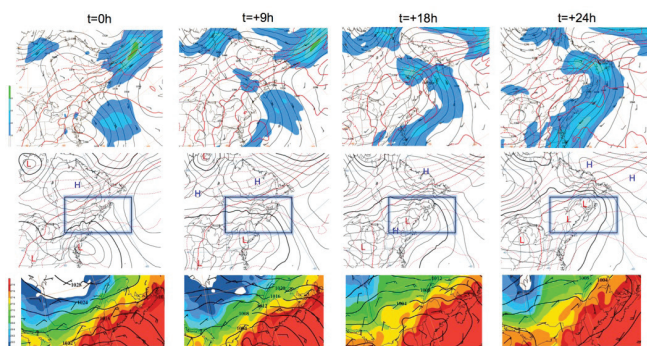


**Figure 4d:** Time evolution of the SN P(SLRV) event. The onset of the event is depicted by  $t = 0$  h, and the phase change occurs in the 4<sup>th</sup> panel. Top row: shaded regions indicate 850hPa wind speeds greater than 30knots ( $15\text{ms}^{-1}$ ), 1000-850hPa thickness (solid black contour interval of 30m), 850 hPa isotherms (contour interval of 4 deg C, with red solid indicating values greater than or equal to 0 deg C, red dashed indicating temperatures colder than 0 deg C), with plotted winds in the standard meteorological convention. Middle row: Sea-level pressures (solid black contour interval of 4 hPa, with bold contour showing the 1008 hPa isobar), and 1000-500hPa thickness (dashed contour interval of 60m, with the bold contour indicating the 5400m value). The blue box identifies the region shown in the bottom row. Bottom row: Surface potential temperature (shaded, in K), sea-level pressure (solid contour interval of 4 hPa), and plotted surface winds of standard meteorological convention.

## DISCUSSION

Given its SW-NE axis, the SLRV orography allows for pressure-driven channeling of cold air, and thus the maintenance of a prolonged FZRA event even while YQB resides in an area of the low that facilitates warm air intrusions aloft. This pressure-driven channeling is predominantly governed by the location and

intensity of the anticyclone, as it is this feature that determines the pressure gradient along the valley. Pairing the wind roses with the meteograms and surface analyses properly depicts this interaction. If conditions aloft do not change, then FZRA will continue as long as the 850 hPa warm air advection continues, and there is enough cold air advection at the surface to offset the effects of latent heat of fusion. At phase change, there is a distinct weakening of winds in each category and a shift in others, depending on where the low pressure system tracks. Lows tracking north of YQB will effect a substantial wind direction shift, whereas wind shifts associated with lows centered south of YQB are less significant. Both the changes in the magnitude and direction of the winds at YQB can be attributed to the loss of pressure-driven channeling. Since low pressure systems within each category are either strengthening or relatively unchanging, we can therefore say this is due primarily to the weakening or translation of the anticyclone. And though the low does obviously play a large role in FZRA precipitation, we focus predominantly on surface flow and the maintenance of CAA. The latter is only possible through the anticyclone, and to first order, we can therefore say that the anticyclone plays an inherent role in maintaining surface cold air and the inversion that facilitates freezing rain. This is also shown in the time evolution of surface potential temperature, with the shading indicating the cold pool of air within the SLRV.

## CONCLUSION

The duration of severe FZRA events in Quebec City is predominantly based on the location and intensity of the anticyclone. This anticyclone provides the basis for pressure-driven channeling which replenishes the cold air required at the surface to maintain a vertical profile conducive to FZRA precipitation. Stationary patterns hold the greatest potential for long duration events, as long as the instability aloft is maintained, as was the example with the great Ice Storm of 1998 (14).

The limitations of this study are similar to those performed by Splawinski *et al.* (2011), and arise in the recording of FZRA accumulations. This method, employed by Environment Canada, does not directly measure accumulations, but rather uses precipitation rates.

However, results still clearly depict the role the anticyclone plays in FZRA events, more so than discussed in past literature. Given this, meteorologists are provided with a novel, insightful approach to forecasting severe FZRA events, which can be used in conjunction with current forecasting techniques. This may provide better forecasts that enable city officials and the general public time to adequately prepare and take all necessary precautions.

## REFERENCES

1. P. Bourgooin, *Weather and Forecasting*, **15**, 583-592 (2000).
2. S. Splawinski *et al.*, *MSURJ*, **6**, 50-55 (2011).
3. J.V. Cortinas Jr., *Mon Weather Rev*, **128**, 3574-3588 (2000).
4. G.I. Huffman, G.A. Norman, *Mon Weather Rev*, **116**, 2172-2182 (1988).
5. J.R. Bocchieri, *Mon Weather Rev*, **108**, 596-603 (1980).
6. S.G.Cober *et al.*, *J Appl Meteorol*, **35**, 2250-2260 (1996).
7. F. Mesinger *et al.*, *Bull Amer Meteor Soc*, **87**, 343-360 (2006).
8. S. Koch *et al.*, *J Appl Meteorol*, **22**, 1487-1503 (1983).
9. Lakes Environmental, 2007: WRPLOT View: Wind rose plots for meteorological data: <http://www.weblakes.com/products/wrplot/index.html>
10. R. Rauber *et al.*, *Weather and Forecasting*, **9**, 183-208 (1994).
11. R. Rauber *et al.*, *J Appl Meteorol*, **40**, 1724-1747 (2001).
12. A. Razy *et al.*, *J Appl Meteorol*, **51**, in press (2012).
13. M. Carrera *et al.*, *J Appl Meteorol*, **48**, 2341-2361 (2009).
14. P.J. Roebber, J.R. Gyakum, *Mon Weather Rev*, **131**, 27-50 (2003).
15. G.M. Ressler, S.M. Milrad, E.H. Atallah, J.R. Gyakum, *Weather and Forecasting*, **27**, in press.

